André Rocha Morais

Licenciatura em Ciências de Engenharia Biomédica

Brain Energy Metabolism in Chronic Hepatic Encephalopathy: an *in vivo* and longitudinal Magnetic Resonance Spectroscopy study on a rat model of Biliary Cirrhosis

Dissertação para obtenção do Grau de Mestre em Engenharia Biomédica

Orientador: Dr. Cristina Cudalbu,
Centre d'Imagerie BioMédicale, CIBM - EPFL
Orientador: Professor Doutor Mário Forjaz Secca,
Professor Associado, FCT - UNL
Co-orientador: Professora Doutora Carla Maria Quintão Pereira,
Professora Auxiliar, FCT - UNL

Júri:

Presidente: Professora Doutora Célia Maria Reis Henriques,
Professora Auxiliar, FCT - UNL
Arguente: Professora Doutora Rita Homem de Gouveia Constanzo Nunes,
Professora Auxiliar, IST - U Lisboa
Vogal: Professora Doutora Carla Maria Quintão Pereira,
Professora Auxiliar, FCT - UNL

FACULDADE DE
CIÊNCIAS E TECNOLOGIA
UNIVERSIDADE NOVA DE LISBOA

Março de 2017

This project was developed in collaboration with:

Centre d'Imagerie Biomédicale (CIBM), École Polytechnique Fédérale de Lausanne (EPFL)

[Brain Energy Metabolism in Chronic Hepatic Encephalopathy: an *in vivo* and longitudinal Magnetic Resonance Spectroscopy study on a rat model of Biliary Cirrhosis]

Ackowledgements

Resumo

A Encefalopatia Hepática é uma síndrome neuropsiquiátrica que pode ter origem em distúrbios cerebrais induzidos pela doença hepática aguda ou crónica. A encefalopatia hepática crónica está associada a cirrose e resulta de uma fibrose hepática progressiva, conduzindo a hipertensão portal e à deterioração da função do fígado. A encefalopatia hepática caracteriza-se por um aumento dos níveis de amónia, denominada hiperamonémia. Uma vez que a encefalopatia hepática conduz a distúrbios cerebrais a nível de osmorregulação, neurotransmissão, antioxidantes e metabolismo energético, foi realizado um estudo longitudinal por ressonância magnética de espetroscopia de hidrogénio num modelo animal tipo C de encefalopatia hepática crónica para analisar alterações a nível de osmólitos cerebrais, energia, neurotransmissores e concentrações de metabolitos antioxidantes. Esta técnica combinada com a ressonância magnética de espetroscopia de fósforo proporcionou uma análise adicional das concentrações dos metabolitos energéticos. Os estudos em questão foram efetuados a 9.4 Tesla. Foi realizada nos modelos animais a ligação das vias biliares e efetuados estudos em diversos intervalos de tempo: 0, 4, 6 e 8 semanas após cirurgia. Relativamente aos osmólitos, verificou-se um aumento significativo na concentração cerebral de Gln, redução de tChol e Ins, bem como uma tendência decrescente na Tau e Cr. Estes resultados sugerem uma resposta osmoregulatória ao aumento de Gln. Relativamente aos neurotransmissores, existiu uma redução em Asp e Glu o que sugere o impacto da hiperamonémia na neurotransmisão, resultante de alterações no fluxo de Gln para o exterior dos astrócitos e impacto na síntese de Glu. A redução dos antioxidantes Asc e GSH é um indicador de stress oxidativo devido á exposição a amónia. Adicionalmente, obervou-se uma ligeira tendência de diminuição observada no γ-ATP, entre outros metabolitos energéticos, que poderá estar relacionada com distúrbios energéticos, no entanto, não justifica a existência de edema cerebral. Globalmente, um aumento dos níveis de concentração de Gln é considerada a principal causa na origem de um ligeiro edema cerebral, de acordo com a Hipótese da Glutamina. O presente estudo vem reforçar a pertinência das abordagens utilizadas e transmitir dados relevantes para estudos futuros.

Palavras chave: Encefalopatia Hepática; doença hepática crónica; hiperamonémia; ligação das vias biliares; osmoregulação; Hipótese da glutamina.

Abstract

Hepatic Encephalopathy is a major neuropsychiatric syndrome that arises from acute and chronic liver disease-induced cerebral disorders. Chronic hepatic encephalopathy is associated with cirrhosis and stems from progressive liver fibrosis, thereby inducing portal hypertension and deterioration in liver function. Hepatic encephalopathy is characterized by increased levels of ammonia, named hyperammonemia. Given that hepatic encephalopathy induces disturbances in cerebral osmoregulation, neurotransmission, antioxidant and energy metabolism, ^{1}H magnetic resonance spectroscopy was performed longitudinally on a rat model of Type C chronic hepatic encephalopathy to assess cerebral osmolyte, energy, neurotransmitter and antioxidant metabolite concentrations. This technique was combined with ^{31}P Magnetic resonance spectroscopy with the purpose of measuring additional energy metabolite concentrations. The studies were carried out at 9.4 Tesla. Rats undergone bile-duct ligation and studies were performed at several stages of disease progression: 0, 4, 6 and 8 weeks after surgery. Results regarding brain osmolyte concentration showed a significant increase in Gln, a decrease in tChol and Ins as well as trends of decrease in Tau and Cr. These results suggest an osmoregulatory response to the increase of Gln. In what concerns to neurotransmission, a decrease was observed in Asp and Glu suggesting that neurotransmission is affected by hyperammonemia which may be an evidence of alterations in the outflow of Gln from astrocytes and interfere with Glu synthesis. The reduction of antioxidants Asc and GSH may indicate oxidative stress due to ammonia exposure. Small trends of decrease observed in γ-ATP and other energy metabolites which may be a sign of energy disturbances but not significant to cause brain oedema. Overall, an increase in concentration levels of Gln it is pointed as the main cause of the minimal brain oedema supported by *Glutamine Hypothesis*. The results of this study are encouraging and relevant for future studies.

Keywords: Hepatic Encephalopathy; chronic liver disease; hyperammonemia; bile-duct ligation; osmoregulation; Glutamine Hypothesis.

Contents

List of Figures

List of Tables

Abbreviations

Asc	Ascorbate
Asp	Aspartate
Ala	Alanine
ALD	Acute Liver Disease
ALF	Acute Liver Failure
BDL	Bile Duct Ligation
Cr	Creatine
CRLB	Cramer-Rao Lower Bounds
CLD	Chronic Liver Disease
CLF	Chronic Liver Failure
Cho	Choline containing compunds
FID	Free Induction Decay
FOV	Field of View
FWHM	Frequency Width at Half Maximum
GABA	γ-aminobutyric acid
GE	Gradient Echo
Glc	Glucose
Gln	Glutamine
Glu	Glutamate
GSH	Glutathione (reduced form)
HA	Hyperammonaemia
HE	Hepatic Encephalopathy
Ins	Myo-inositol
ISIS	Image selected *in vivo* spectroscopy
Lac	Lactate
MRI	Magnetic Resonance Imaging
MRS	Magnetic Resonance Spectroscopy
NAA	N-Acetyl Aspartate
NAAG	N-Acetyl Aspartate Glutamate
OVS	Outer Volume Suppression
PCr	Phosphocreatine
PDE	Phosphodiesters
Pi	Inorganic Phosphate
PME	Phosphomonoesters

ppm	parts per million
ROI	Region of Interest
SE	Spin Echo
SNR	Signal to Noise Ratio
Tau	Taurine
tCho	Total Choline
tCr	Total Creatine
VAPOR	Variable Pulse Powers and Optimised Relaxation Delays
VOI	Volume of Interest

Chapter 1

Hepatic Encephalopathy and Chronic Liver Disease

1.1 Introduction

Hepatic encephalopathy (HE) is a major neuropsychiatric disorder that arises from acute and chronic liver disease (ALD, CLD). It is characterized by a spectrum of symptoms such as motor deficits, behavioural disturbances and cognitive impairment, which have a significant effect on the quality of life. HE leads to an altered mental status, causing irreversible damage in the central nervous system (CNS) and in the worst-case scenario coma and death (Butterworth, 2003).

The definition of HE is based on both the hepatic abnormality, categorized into three types (A, B and C), and the characteristics of neurologic manifestations in chronic liver disease. Type A is associated with acute liver failure (ALF), a rapid necrosis that leads to the severe deterioration of liver function and hence of the mental status. Type B is associated with portal-systemic bypass without liver disease, in which gastrointestinal blood enters directly into the systemic circulation without passing through the liver, thus exposing the brain to gut-derived toxins. Type C is associated with chronic liver disease, usually in the setting of alcohol-induced cirrhosis, and portal-systemic shunting. Other main etiologies of cirrhosis are liver inflammations due to viral infections or accumulation of fat deposits in the liver (Bosoi and Rose, 2013a, Ferenci et al., 2002).

The severity of chronic HE is further divided into minimal (MHE) and overt (OHE). MHE appears as the mildest form of HE, characterized by subtle neuropsychological alterations as mild cognitive and psychomotor dysfunctions. These changes are only detectable using psychometric tests and have no clinically evident symptoms. Despite the lack of an approved symptomatology, OHE presents clinical evidences in which the severity is graded according to the West Haven criteria. Accordingly, patients are classified into four grades with symptoms ranging from shortened attention span (grade I) to coma (grade IV) (Felipo, 2013).

The aim of the present thesis was to study *in vivo* the longitudinal metabolic alterations involved in HE, mainly regarding the brain energy metabolism. It is known that HE affects both adults and children, therefore, this study focused on the adult version of an animal model of chronic HE (Type C). Since 30 to 50% of the population with cirrhosis present this common and severe disorder (Munoz, 2008), it becomes increasingly important to achieve a better understanding of the

mechanisms involved.

1.2   Pathogenesis

Ammonia is considered to be the main culprit in HE (Bosoi et al., 2014). It is primarily produced within the gut by urease-positive bacteria during protein digestion and deamination. Then, it is released in the liver through the portal venous system and detoxified in the urea cycle to urea, to be maintained at low concentrations (50-150μM in preterm neonates, 50-75μM in term neonates and < 50μM in adults) (Braissant, 2010). In the presence of liver disease, ammonia levels increase as a result of a deficient urea cycle leading to the onset of hyperammonemia (HA). The excess ammonia passes into the blood circulation and enters the brain through the blood-brain barrier (BBB), reaching toxic levels to the central nervous system (CNS) (Bosoi and Rose, 2013a).

Despite the fact that there is no effective urea cycle in the brain, ammonia is maintained at low concentrations. There are two mechanisms which enable the brain to metabolize ammonia. Firstly, the reductive amination of α-ketoglutarate to glutamate (Glu) by the glutamate dehydrogenase reaction (GDH). Secondly, the action exclusively in the astrocytes of glutamine synthetase (GS) that converts Glu and ammonia to Gln, which is the main pathway for ammonia detoxification (Brusilow et al., 2010). After that, the Gln produced goes into the adjacent neurons where it is converted into Glu by glutaminase (GA). Accordingly, studies have shown a significant increase in brain glutamine (Gln) following the increase in cerebral ammonia (Singh et al., 2014, Braissant et al., 2012).

Regardless of the etiology, the main pathogenic mechanisms in HE (Fig. 1.1) are: amino acid disturbances (glutamine, glutamate, arginine), changes in neurotransmission (glutamatergic, cholinergic, serotoninergic systems), brain energy disturbances (in detail in section 1.3.3), modifications in nitric oxide synthesis (NOS), deficiency of axonal and dendritic growth, disruption of transduction pathways and apoptosis (Cagnon and Braissant, 2007).

The main pathway for ammonia detoxification in the brain is the synthesis of Gln from Glu and ammonia. In that sense, three main hypothesis regarding the pathogenesis of HE have been proposed:

Glutamine Hypothesis: There is an increased glutamine synthesis in the brain due to hyperammonemia. It is suggested that glutamine acts as an osmolyte and its accumulation leads to a shift of water into the cells and cell swelling (Brusilow et al., 2010). Studies in CLD reported that following to the increase in glutamine within the astrocytes there is a reduction in other osmolytes such as myo-inositol (Ins), choline (Cho) and taurine (Tau). This may indicate a compensatory response in order to maintain the osmotic balance, thereby minimizing intracranial pressure and brain oedema (Zwingmann, 2007). However, this hypothesis has been questioned as no correlation was found between Gln concentration and cell swelling over time (Rama Rao and Norenberg, 2014).

Trojan Horse Hypothesis: The synthesized glutamine is transported into the mitochondria where it is metabolized by phosphate-activated glutaminase (PAG) to glutamate and ammonia. In this way, the excess glutamine acts as a carrier across the mitochondrial membrane, thereby yielding high levels of ammonia. This will interfere with the normal mitochondrial function, giving rise to excessive reactive oxygen species (ROS), inducing the mitochondrial permeability transition (MPT)
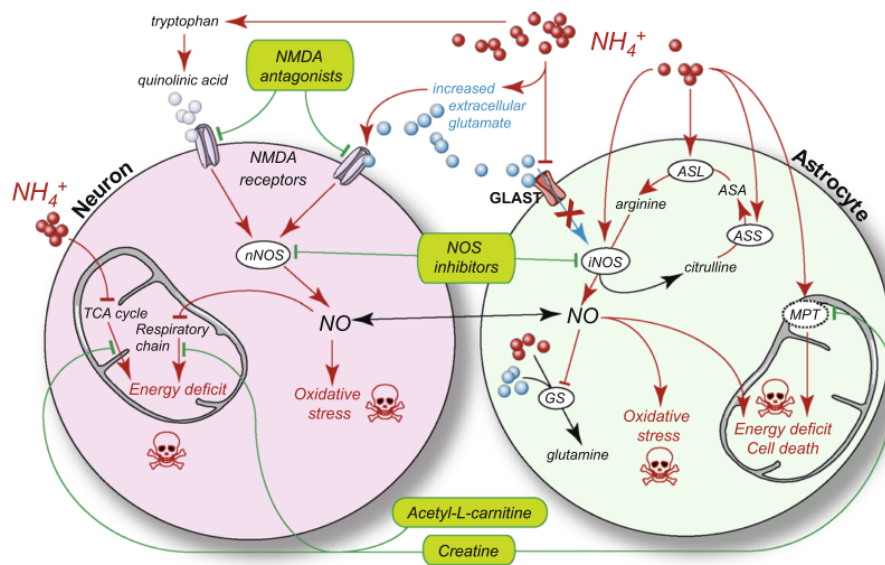
Figure 1.1: Description of the neurotoxicity of ammonia. Illustrated in red are the toxic effects to the astrocytes and neurons, in particular oxidative stress, cell death in the CNS and energy deficit through hampering of the TCA cycle and opening of the MPT (Braissant, 2010).

and thus originating astrocytes dysfunction such as oxidative stress and cell swelling (Brusilow et al., 2010, Albrecht and Norenberg, 2006). However, the presence of PAG in astrocytes in accordance with this hypothesis was questioned, as it is thought to be present only in neurons (Rama Rao and Norenberg, 2014).

Transporter Hypothesis: During the process of ammonia removal Gln is synthesized in astrocytes and released into the brain extracellular space via the small neutral amino acid transporter 5 (SNAT5). Subsequently, it is captured by neurons to produce Glu. This hypothesis suggests that Gln is trapped within the astrocytes as a consequence of down-regulation of SNAT5 in acute liver failure (ALF), which may lead to cell swelling/brain oedema. Additionally, impairment of glutamatergic (excitatory) neurotransmission leads to excessive neuroinhibition, as a result of the restricted transfer of Gln to the adjacent nerve terminal (where Gln serves as immediate precursor for the releasable/transmitter pool of Glu) (Desjardins et al., 2012).

1.3   Current State of Research

1.3.1   Importance of *in vivo* studies of CLD for the study of HE

In order to find neuroprotective strategies for HE, a better understanding of the neurotoxicity of ammonia is imperative. There is a lack of *in vivo* studies in this field, mainly those longitudinally focused on glutamine kinetics, CNS osmolytes and metabolites, oedema development, brain energy metabolism, antioxidant and neurotransmitter changes all together on one model of HE in CLD. So far, these studies were mainly carried out by the CIBM/LIFMET group.

The Bile Duct Ligation (BDL) model is the animal model used in these studies. The rats are most commonly used since there is, for instance, a lot of anatomical information already verified and

the costs are much lower when compared with larger animals. In the present model, the rats undergo surgery and the bile duct is ligated (Jover et al., 2006). The operation triggers biliary cirrhosis and induces a range of symptoms, such as: jaundice, portal-systemic shunting, portal hypertension, hyperammonemia, dysfunction of the immune signal and bacterial translocation as well as motor and memory deficits (Butterworth et al., 2009). The control rats are sham-operated.

The BDL rat is a model of CLD that associates HE with cirrhosis and portal hypertension, i.e. HE type C. It has been certified by the ISHEN (International Society for Hepatic Encephalopathy and Nitrogen Metabolism) commission.

1.3.2   Brain oedema and osmolytes in chronic HE

Brain oedema is characterized by an accumulation of water within the cerebral tissue (intracellular and/or extracellular), which occurs in the setting of an osmotic gradient. It is a pathological feature of HE in both ALF and CLD that generates an increase in brain volume and hence may enhance intracranial pressure (ICP) leading to brain stem herniation and death (Bosoi and Rose, 2013a).

1.3.2.1   Human subjects

Studies in patients with chronic HE using ^{1}H MRS have shown changes in brain osmolytes such as inconsistent reductions in total choline (tCho) and myo-inositol (Ins). These changes suggest a cerebral osmotic imbalance and are likely to reflect an osmoregulatory mechanism that occurs following to Gln accumulation in astrocytes, as a result of the increased ammonia levels (Keiding and Pavese, 2013). Furthermore, other studies reported brain oedema in cirrhotic patients (Rovira et al., 2008), extracellular mild brain oedema in CLD (Kale et al., 2006) and supported the view that ammonia contributes to cerebral oedema in HE by increasing brain water content (Mardini et al., 2011).

1.3.2.2   Animal subjects

Studies carried out using an *in vitro* model of cultured embryonic rat brain cell aggregates exposed to ammonia, reported an increase in brain Gln and ammonia levels (Bachmann et al., 2004). Furthermore, BDL rats showed and increase in brain Gln and a decrease in osmolytes together with the progression of liver disease. It was also observed a small rise in the amount of cortical water (Chavarria et al., 2013).

So far there has only been a few *in vivo* studies in living experimental animal models of CLD performed in BDL rats. Recent studies carried out at CIBM/LIFMET, characterized *in vivo* and longitudinally the progression of HE over 8 weeks in BDL rats, a model of CLD. Increased Gln was observed after each weekly measurement as well as a significant decrease in Ins, tCho and Tau after 8 weeks in adult rats and apparent diffusion coefficient (ADC) values were higher, suggesting low-grade oedema despite the osmoregulatory response (Cudalbu, 2012). Also histology of the brains was done and revealed swelled astrocytes.

It has previously been shown that cultured astrocytes exposed to lactate exhibit swelling (Ringel et al., 2006). Recent studies suggested for the first time that increased brain levels of lactate and not Gln have a major impact in the onset of brain oedema in CLD, which might be also correlated with the severity of HE. The synthesis of lactate and glutamine was observed to be significantly

higher in the brains of BDL rats when compared with SHAM-operated controls and it was proposed a 'low-grade' oedema for CLD. Additionally, increased lactate production induces osmotic stress and also generates more water per ATP produced than oxidative phosphorylation. The present study also suggest that impaired osmoregulatory response may contribute to the onset of brain oedema in CLD (Bosoi et al., 2014).

Whether the increase in brain lactate is a cause or a consequence of pathophysiological mechanisms remains to be established. On one hand, it is believed that there is a correlation between hyperlactatemia and ICP in ALF and the reasons for this increase have been previously mentioned to be cerebral hypoperfusion, decreased cerebral oxygenation and ammonia-induced inhibition of α-ketoglutarate dehydrogenase. On the other hand, it is also stated that the lactate/pyruvate ratio is maintained, the cerebral α-ketoglutarate dehydrogenase is undisturbed and there is no significant impairment of brain mitochondrial complex activities in late stages of ALF. Taken together, it seems that increased lactate levels are a consequence of pathophysiological mechanisms rather than its cause and therefore the suggestion to consider it as a therapeutic target and inhibit its synthesis requires discussion, since lactate is an important energy resource for the brain (Oria and Jalan, 2014).

The liver has a key role in oxidative stress regulation. Oxidative stress is defined as an imbalance between the production of reactive oxygen species (ROS) and antioxidant defence, which may lead to cellular dysfunction. It is a direct consequence of liver disease and is triggered by a reduction in liver protein synthesis, thus diminishing the antioxidant capacity (Bosoi and Rose, 2013b). Studies have suggested a synergistic role between ammonia and oxidative stress in the pathogenesis of brain oedema in BDL rats. An increase in brain water was only observed when increasing brain ammonia by chronic hyperammonemia acted together with oxidative stress, suggesting that factors other than ammonia are involved in the pathogenesis of brain oedema and HE during CLD (Bosoi et al., 2012).

1.3.3   Brain Energy Metabolism in HE

The brain is formed by two main cell types, the neurons and glial cells. The neurons are the core components of the CNS as they process and transmit information through electrochemical signals. The glial cells also take part in the neurotransmission process, provide support and protection to the neurons and play an important role in the brain metabolism. Ammonia homeostasis has been shown to be crucial for normal brain function. In that sense, an outline will be provided of the effects of high levels of ammonia and the main metabolic processes involved (Bak et al., 2012).

1.3.3.1   Changes in Glucose utilization

The major substrate for energy production is glucose (Mckenna et al., 2012). Patients with chronic HE have consistently showed a decreased cerebral metabolic rate for glucose (CMRglc) (Rama Rao and Norenberg, 2012), while positron emission tomography (PET) studies reported a decrease of glucose utilization especially in the frontal cortex and an increase in the hippocampus, basal ganglia and cerebellum with increasing grade of HE (Weissenborn and Lockwood, 2012). Whereas studies in different animal models of HE are ambiguous, cultured neurons and astrocytes treated with ammonia showed increased glucose utilization (Rama Rao and Norenberg, 2012).

1.3.3.2   Changes in Glycolysis

Glucose metabolism described in Fig. 1.2 can be separated into two parts, the glycolytic and oxidative pathways. The first takes place in the cytosol whereas the second is located in the mitochondria and consists of pyruvate oxidation followed by the oxidation of acetylCoA in the tricarboxylic acid (TCA) cycle. Initially, glucose is phosphorylated to glucose-6-phosphate by hexokinase (HK), subsequently being metabolised to pyruvate while two molecules of NAD^+ are reduced to NADH. Either the latter is reoxidized via reduction of pyruvate to lactate by lactate dehydrogenase (LDH) or is transferred to the mitochondria via the malate-aspartate shuttle (MAS). Then, it will be oxidized in the electron transport chain for oxidative phosphorylation. This mechanism enables the cytosolic level of NAD^+ to be maintained. Finally, each molecule of glucose metabolised gives rise to two molecules of pyruvate with a net synthesis of two molecules of ATP (Bak et al., 2012).

Changes in cerebral glycolysis were reported based on increasing levels of glucose followed by reduced pyruvate levels in the spf model of congenital hyperammonemia (Rao and Norenberg, 2001). It was found that the generation of lactate from glucose sharply increased by exposure to ammonia using neurons in co-culture with astrocytes (Leke et al., 2011). Furthermore, significant increases in the activities of several glycolytic enzymes suggested an enhanced rate of glycolysis. Unlike to that expected, the operational rate of the TCA cycle did not increase as the pyruvate generated was converted to lactate (Rama Rao and Norenberg, 2012).

1.3.3.3   Changes in the TCA cycle

Oxidative metabolism begins when pyruvate from glycolysis enters the mitochondria where it is either oxidized to acetylCoA by pyruvate dehydrogenase (PDH) or carboxylated to oxaloacetate by pyruvate carboxylase (PC). The TCA cycle, shown in Fig. 1.3, starts with the condensation of acetylCoA with oxaloacetate to form citrate. Citrate is converted to α-ketoglutarate, which is decarboxylated to succinyl-CoA and later to succinate. At the complex II of the respiratory chain succinate is oxidized to fumarate and then converted into malate. Either the latter can be oxidized to oxaloacetate or it can be converted to pyruvate. Furthermore, the amino acids aspartate and glutamate stem from oxaloacetate and α-ketoglutarate (Mckenna et al., 2012).

Studies in mitochondria isolated from cerebral cortex reported inhibition of α-ketoglutarate dehydrogenase (α-KGDH) by ammonia (Lai and Cooper, 1991). Further studies carried out in several animal models of chronic HE and hyperammonemia showed a decrease in the operational rate of the TCA cycle due to the removal of α-ketoglutarate for ammonia detoxification. As a consequence of the inhibition of the TCA cycle, a reduction of the oxidative phosphorylation is expected and hence a depletion of ATP and other high energy metabolites. Furthermore, α-KGDH and malate dehydrogenase inhibition by ammonia might affect the transfer of reducing equivalents through the MAS (Rama Rao and Norenberg, 2012). The MAS has a key role in maintaining the cytosolic level of NAD^+ as a low $NADH/NAD^+$ ratio is crucial for continuation of glycolysis. Thus, MAS is responsible for transferring reducing equivalents from the cytosol to mitochondrial electron transport chain and subsequent oxidative phosphorylation. One proposed explanation for energy disturbances in HE is a dysfunction of the MAS (Rao and Norenberg, 2001).
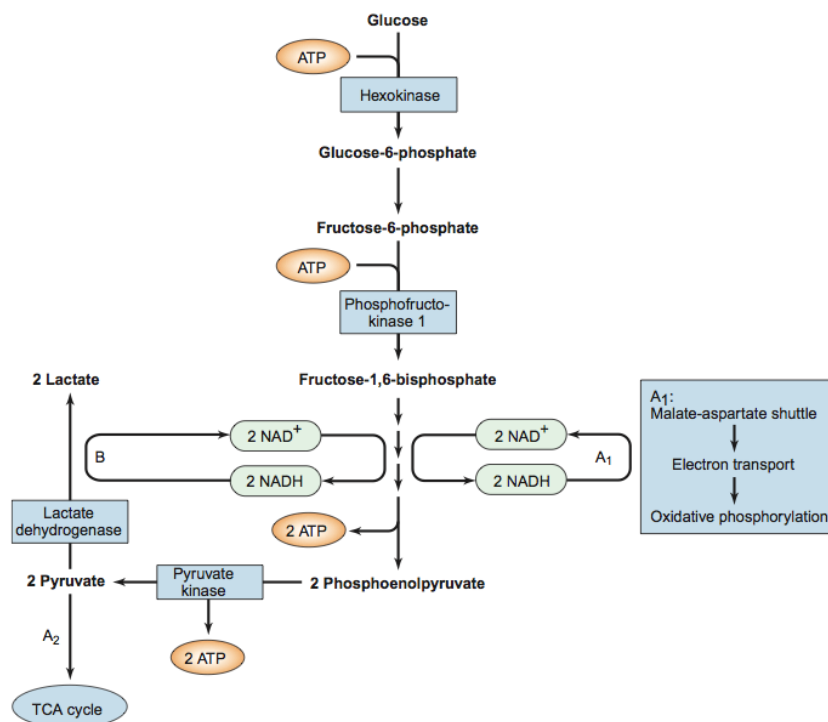
Figure 1.2: Schematic outline of glycolysis, aerobic (A_1 and A_2) and anaerobic (B), with production of pyruvate and regeneration of NAD^+. Pyruvate is subsequently metabolised via the TCA cycle (A_2). The NADH produced can be oxidized in the lactate dehydrogenase reaction (B) or its reducing equivalent can be transferred to the mitochondria via the MAS and subsequently be oxidized in the electron transport chain for oxidative phosphorylation (A_1). When glycolytic flux exceeds that of the TCA cycle, lactate can also be produced under aerobic conditions (Mckenna et al., 2012).

1.3.3.4 Changes in Oxidative Phosphorylation

In order to maintain the TCA cycle, the reduced co-enzymes produced in the oxidative processes must be reoxidized. This is accomplished in the enzyme complex I of the mitochondrial respiratory chain for NADH, whereas for $FADH_2$ it takes place in the complex II. The complexes, coenzyme Q (CoQ) and cytochrome C (Cyt C) transport the electrons that will generate O_2, which is reduced to H_2O in complex IV. This creates a proton gradient along the inner membrane powering synthesis of ATP in complex V. Hence, most of the ATP from glucose metabolism is produced.

Studies carried out in mitochondria isolated from cerebral cortex reported an inhibition of complex III by addition of ammonia (McKhann and Tower, 1961). Congenitally chronic hyperammonemic spf-mice showed an inhibition of the complex IV (Cyt C oxidase) activity (Rao et al., 1997). In the same model, a higher degree of inhibition of the complexes II and III was observed in synaptosomes when compared to non-synaptic mitochondria (Qureshi et al., 1998). Furthermore, other studies showed decreased brain levels of both ATP and phosphocreatine in porta-caval shunted rats as a model of chronic HE, acutely injected with ammonium acetate (Hindfelt et al., 1977). Accordingly,
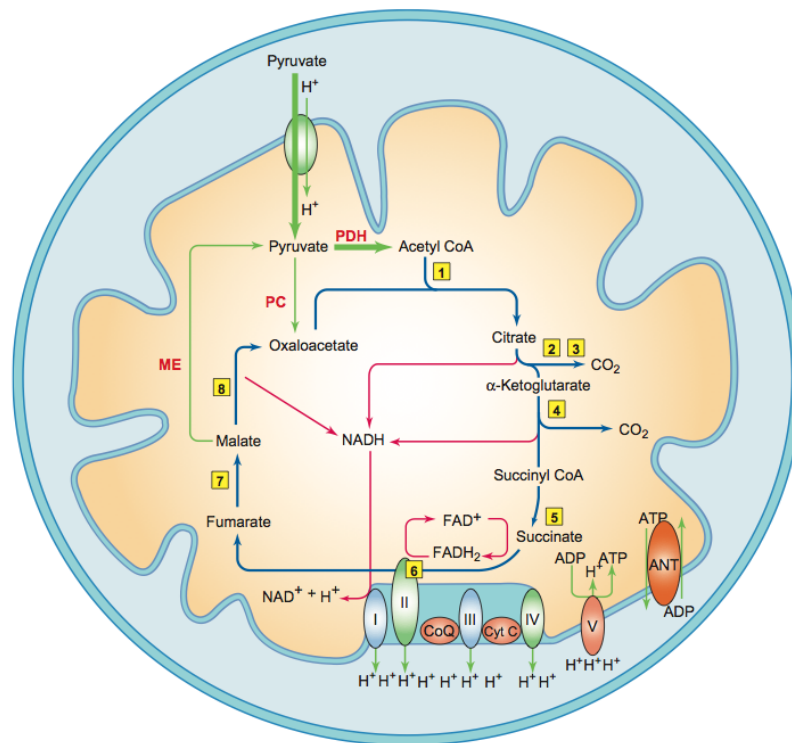
Figure 1.3: Schematic outline of the TCA cycle and oxidative phosphorylation. The enzymes that take part in the TCA cycle are (1) citrate synthetase, (2) aconitase (3) isocitrate dehydrogenase (4) α-ketoglutarate dehydrogenase complex, (5) succinyl-CoA synthetase, (6) succinate dehydrogenase, (7) fumarate hydratase, (8) malate dehydrogenase (Mckenna et al., 2012).

reduced ATP levels after exposure to ammonia were reported in cultured astrocytes (Haghighat and McCandless, 1997, Zwingmann and Leibfritz, 2005). Therefore, decreased enzyme complexes activity could be one possible cause of the ATP reduction (Rao and Norenberg, 2001).

1.3.3.5   Changes in High Energy Metabolites

The energy charge of a cell is related to the concentrations of high-energy phosphates, particularly ATP (Zwingmann, 2007). Studies conducted in brains of the spf-mice model of chronic hyperammonemia showed a decrease in brain ATP levels (Rao et al., 1997). Accordingly, decreased levels of ATP were also observed in cultured astrocytes treated with ammonium chloride (Haghighat and McCandless, 1997, Haghighat et al., 2000). These changes in mitochondrial energy metabolism in chronic HE could stem from inhibition of oxidative phosphorylation or its increased consumption (Xue et al., 2010).

1.3.3.6   Changes in Oxidative/Nitrosative Stress (ONS)

Free radical production was found to increase in a dose-dependent manner in cultured astrocytes exposed to ammonia (Murthy and Rao, 2001). Studies described reversible and irreversible damage to mitochondrial respiratory chain enzymes, specially to Cyt C oxidase, caused by excess production of

nitric oxide (NO) (Heales et al., 1999). Additionally, NO has been shown to have a negative impact on the mitochondria (Stewart et al., 2000) which may include lipid oxidation of the mitochondrial membrane (Gutierrez et al., 2006). On the other hand, it is possible that ONS exists due to mitochondrial dysfunction as a result of the MPT (Zorov et al., 2006).

1.3.3.7 Mitochondrial permeability transition (MPT)

The MPT is defined as an increase in the permeability of the inner mitochondrial membrane to small solutes (<1500Da). It results from the opening of a permeability transition pore (PTP) mostly triggered by increasing mitochondrial Ca^{2+} (Kristal and Dubinsky, 1997). Consequently, the membrane potential generated by the release of protons from the electron transport chain is lost thus causing osmotic swelling of the mitochondrial matrix, circulation of metabolites through the inner membrane, impaired oxidative phosphorylation, interruption of ATP synthesis and production of reactive oxygen species (ROS) (Rama Rao and Norenberg, 2012).

It was shown that ammonia increases the mitochondrial permeability and collapses the membrane potential in cultured astrocytes but not in cultured neurons (Bai et al., 2001). Glutamine production was also suggested to play an important role in this process. Studies in cultured astrocytes reported that DON, an inhibitor of phosphate-activated glutaminase, blocked the ammonia-induced MPT (Rama Rao et al., 2005). Furthermore, the collapse of the membrane potential by ammonia was stopped due to methionine sulfoximine (MSO), an inhibitor of glutamine synthetase (GS). Finally, it is known that both oxidative stress and mitochondrial dysfunction are two important pathogenic mechanisms in HE. Either oxidative stress induces the MPT or is a consequence of the MPT when following ammonia treatment remains elusive (Rao and Norenberg, 2001).

1.3.3.8 Changes in Glutamate

Glutamate is the main excitatory neurotransmitter in the CNS and a fuel for astrocytes, taking part in several reactions of the brain energy metabolism. Brain glutamate was shown to be reduced in several models of HE. Together with aspartate, glutamate is present in the MAS where its production was suppressed. Moreover, addition of glutamate or aspartate normalized the MAS. Taken together, these results underline the importance of glutamate in the pathogenesis of HE (Rao and Norenberg, 2001).

1.3.3.9 Changes in Lactate

Lactate is formed through glycolysis. Its production is ruled by the concentration of lactate, pyruvate and $NADH/NAD^+$ ratio, catalysed by LDH which is found in both neurons and astrocytes. Patients with chronic HE showed increased levels of brain lactate, probably associated with the progression and severity of HE. Whether the BBB is permeable to lactate remains unclear (Rose, 2010). Other studies reported increased levels of cerebral lactate in cultured astrocytes after ammonia treatment together with a decreased pyruvate/lactate ratio (Haghighat and McCandless, 1997, Kala and Hertz, 2005). These changes may result either from changes in lactate production/uptake or increased glycolysis due to energy impairment. Following to the latter case, there is an increase in pyruvate levels which is normally converted to acetylCoA and enters the TCA cycle. This conversion occurs via PDH, which

was shown to be inhibited by ammonia. Consequently, it may affect the rates of the TCA cycle and decrease reducing equivalents in the electron transport chain where ATP is produced (Rama Rao and Norenberg, 2012).

1.3.3.10   Changes in Creatine

The creatine (Cr)/ Phosphocreatine (PCr)/ Creatine kinase (CK) system acts in maintaining the energy levels through buffering and transport of high-energy phosphates. In the CNS, Cr plays a key role in axonal and dendritic growth, neurotransmitter release and maintenance of membrane potential. Accordingly, studies have shown that a decrease of Cr inhibited axonal growth. Furthermore, a reduction in Cr and PCr levels was reported in brain cells cultures, supporting the theory that ammonia exposure leads to an energy deficit (Cagnon and Braissant, 2007).

1.3.4   Techniques for Analysis

Magnetic Resonance Imaging (MRI) and Magnetic Resonance Spectroscopy (MRS) are extremely important non-invasive techniques for diagnosis. At high magnetic fields (9.4T), ^{1}H MRS enables the longitudinal study of 20 brain metabolites and focus on osmoregulation (Gln, Ins, Tau, tCho), neurotransmission (Asp, Glu) and energy metabolism (Ala, Lac, Cr, PCr). In turn, ^{31}P MRS allows to go further on energy metabolism tracking the concentration of PCr, inorganic phosphate P_i, adenosine triphosphate (α, β and γ-ATP), phosphomonoesters (PME) and phosphodiesters (PDE).

In order to have a more solid study, other techniques can be combined with MRI and MRS. By performing histology of the brain it becomes possible to analyse changes in the structure of the tissues. To accomplish that, the brain is taken out right after the rat being sacrificed, preserved in formalin and kept cool or frozen until the microscopic examination is performed. Since the water content of the brain might change, the wet/dry weight method (Chan and Fishman, 1985) can be applied.

As chronic HE stems from motor and cognitive impairment, open field and Y-Maze behavioural tests (gon Lee et al., 2008) can be performed to search for motor and cognitive impairment and evaluate the impact of emotional and behavioural disturbances in the quality of life of the subject. However, for these tests to be accurate there are several aspects that have to be taken into account, e.g. isolation, regarding the laboratory environment (Balcombe, 2006). For example, it was reported that rats isolated during their juvenile stage show opposite behaviour on openfield in comparison with rats isolated during their postmaturity. However, more tests are needed since the differences cannot be interpreted by a simple unitary explanation. Moreover, subjects should be handled before the tests to get familiar with the experimenter (Karim and Arslan, 2000, Dalrymple-Alford and Benton, 1984).

1.4   Aims

The pathogenesis of brain oedema in CLD is of some debate since it is still unclear if brain energy metabolism is affected in chronic HE as it is in acute HE. The aims of this thesis are to study *in vivo* and longitudinally the changes in metabolites concerning to osmoregulation, energy metabolism and

brain oedema using a BDL adult rat model of CLD. Therefore, ^{1}H and ^{31}P MRS techniques will be used in order to help determining the pathogenesis of HE.

Chapter 2

Nuclear Magnetic Resonance, MRI and MRS

2.1 Nuclear Magnetic Resonance

Nuclear Magnetic Resonance (NMR) is the basic phenomenon associated with the techniques of spectroscopy (MRS) and imaging (MRI), which are powerful tools to assess physical and biochemical information *in vivo* and non-invasively.

The primary concept of NMR is based on the interaction magnetic fields with magnetic moments of nuclei of different atoms. The magnetic moment is correlated with an angular momentum of these nuclei, named nuclear spin, which value is defined by a spin number. The spin quantum number I is $1/2$ for electrons, neutrons and protons. Only nuclei with an odd number of either protons and neutrons have a nonzero spin and magnetic moment are therefore detected in NMR. Moreover, nuclei with $I > 1/2$ (such as ^{1}H,^{31}P, ^{13}C and ^{15}N) have an electrical quadrupole moment, thus affecting the nuclear magnetic moment and being more favourable for practical magnetic resonance. Therefore, as NMR is mostly used on nuclei with $I = 1/2$, the spin dynamics is then reduced to two energy states.

Even though quantum mechanics is the only theory which enables a quantitative description, a classical approach can be useful to visualize the NMR phenomenon in a frame of reference. Take a nucleus with constant angular momentum ($\vec{L}$), i.e. rotating on its own axis with constant velocity at a distance $\vec{r}$, without interacting with any external force. In a classical point of view, if the nucleus carries an electrical charge and is rotating, it creates a current loop and a magnetic field arises. This magnetic field is characterized by the magnetic dipole moment ($\vec{\mu}$), which depends on the current and the area of the loop. Quantum mechanics describes angular momentum by its quantized amplitude and certain discrete orientations for a given direction determined by the magnetic quantum number m. The component of the angular momentum vector in the z-direction is given by the following expression:

$$L_z = \hbar m \tag{2.1}$$

where m can have the values given by $I, I - 1, I - 2, ..., -I$. The magnetic dipole moment is given by:

$$\vec{\mu} = \left(\frac{e}{2m}\right)\vec{L} = \gamma\vec{L} \tag{2.2}$$

where m is the mass of the nucleus and γ corresponds to the gyromagnetic ratio. The latter is an intrinsic characteristic of each nucleus and equals to 42.578 and 17.252 MHz/T for protons and phosphorus, respectively. In a macroscopic ensemble of spin 1/2 nuclei, they are oriented randomly in such a way that the net magnetisation, i.e. vector sum of the magnetic moments, is zero. When placed in a static magnetic field ($\vec{B}_0$) oriented along the z direction, each nucleus interacts with it through the magnetic moment. Therefore, there are two possible energy states: a low energy state with $m = +1/2$ ($\vec{\mu}$ parallel with $\vec{B}_0$) and a high energy state with $m = -1/2$ ($\vec{\mu}$ antiparallel to $\vec{B}_0$), the so-called α and β spin states, respectively. The energy difference between these two spin states increase linearly with the static magnetic field and is known as Zeeman splitting, given by:

$$\Delta E = \gamma \hbar B_0 \tag{2.3}$$

The resonance condition can be achieved through the application of an oscillating magnetic field perpendicular to μ_z with a frequency ν_0, such that the energy splitting between the two spin states corresponds to the one of the electromagnetic wave, which is given by:

$$\Delta E = h\nu_0 \tag{2.4}$$

Combining Equations (2.3) and (2.4) will give the Larmor equation:

$$\omega_0 = \gamma B_0 \tag{2.5}$$

where ω_0 is known as the Larmor frequency, which is also the excitation frequency necessary to change the spins from the parallel to the antiparallel state. As a consequence of the slight difference between energy levels, the populations of spins among the two orientations are determined by the Boltzmann equation:

$$\left(\frac{n_\alpha}{n_\beta}\right) = e^{\frac{\Delta E}{kT}} = e^{\frac{h\nu}{kT}} \tag{2.6}$$

where n_α and n_β correspond to the number of spins in the α and β state respectively, k is the Boltzmann constant and T the system temperature in Kelvin. Temperature is not a flexible parameter since *in vivo* studies have to be performed at body temperature, however, the macroscopic magnetization can be increased by using a higher external magnetic field since the higher it is, the greater the n_α. The nuclei in a static magnetic field with a magnetic moment that differs from zero, tend to have the orientation with the lowest energy. This orientation is disturbed by thermal energy making the orientation of the nuclear moments almost random in the magnetic field with increased tendency for the lower energy state. Such orientation in these conditions gives rise to a vector sum of individual nuclear magnetic moments, named macroscopic magnetisation, which is aligned with the direction of the static magnetic field when it is in equilibrium. If they are not parallel, the magnetisation will precess about the direction of the static magnetic field with an angular frequency, i.e. Larmor Frequency. Therefore, it is only possible to detect the magnetisation when it is not static, which means it precesses about the direction of the magnetic field. In order to measure the magnetisation, tilting it is necessary from being parallel and lead to its precession, however, this is not technically feasible and then arises the use of the concept of resonance (Mlynarik, 2016). Although there are more spins in the lower energy states, the slight difference between the two spin states makes the resultant magnetisation ($\vec{M}_0$) very small and NMR a rather insensitive technique in comparison with other types of spectroscopy. The net magnetisation is proportional to the number of spins, the field strength and the gyromagnetic ratio. Indeed, there is also a component of the nuclear angular momentum transverse to $\vec{B}_0$. This component is responsible for the existence of a torque that makes

$\vec{\mu}$ precess around $\vec{B}_0$ at a frequency described by Equation (2.5). Thus, for nuclei of spin 1/2, the magnetic moments will form a cone shaped distribution while in steady state (Fig. 2.1). This shape arises as a result of the angle $\theta = 54.74°$ between the nuclear magnetic moment and the external field, relative to $+z$ and $-z$ axis for $m = +1/2$ and $m = -1/2$, respectively:

$$cos(\theta) = \frac{m}{\sqrt{I(I+1)}} \tag{2.7}$$
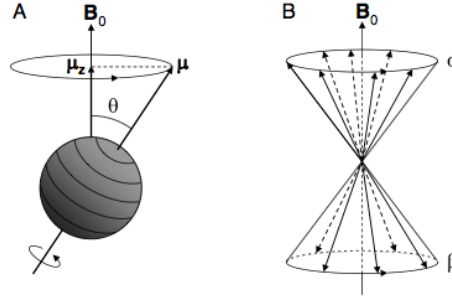
Figure 2.1: A) A nuclear spin precessing in the presence of $\vec{B}_0$ at an angle θ and amplitude along z quantized. B) Consequently, the spins form a cone-shaped distribution among two possible orientations (Graaf, 2007).

2.1.1 Excitation

In order to measure nuclear magnetisation, the steady-state needs to be perturbed by rotating the net longitudinal vector towards the transverse plane (Fig. 2.2). This is accomplished by applying a second magnetic field ($\vec{B}_1$) using a transmit RF coil, the so-called RF pulse, which is perpendicular to $\vec{B}_0$ and oscillates in the radio frequency range (RF) at the Larmor frequency. Therefore, the magnetisation will precess about both magnetic fields with respective angular frequencies of $\omega_0 = \gamma B_0$ and $\omega_1 = \gamma B_1$, and its final position will depend on the amplitude and duration of $\vec{B}_1$. NMR not only is non invasive but also non-ionising due to the radio wave frequency. In order to simplify further analysis, a rotating reference frame around $\vec{B}_0$ at the Larmor frequency can be used. In that case, $\vec{M}_0$ is visualized as a stationary vector in the same direction as the external magnetic field and $\vec{B}_1$ as a static magnetic field in the transverse plane.

Depending on the duration of $\vec{B}_1$, the magnetisation can be tilted towards the transverse plane or even inverted to the $-z$ axis, being described by the nutation angle. These two situations correspond to the so-called 90° excitation and 180° inversion RF pulses, respectively. The randomly distributed spins will experience two effects due to the $\vec{B}_1$ field. Firstly, the closer the nutation angle is from 90°, the more equally distributed the two spin states will be. Following the RF pulse, the magnetisation experiences only the external magnetic field in such a way that the spins come into a state of phase coherence and the transverse magnetisation arises. Considering the rotating frame, the magnetisation is given by:

$$M_z = M_0 \cos\theta \tag{2.8}$$

$$M_{xy} = M_0 \sin\theta \tag{2.9}$$
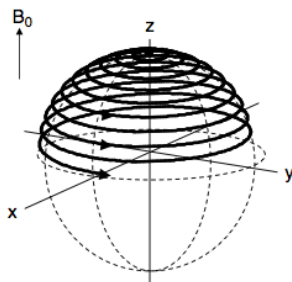
Figure 2.2: Excitation of the magnetisation in the laboratory reference frame. It results in a
rotation towards the transverse plane at the Larmor frequency (Graaf, 2007).

where M_z is the longitudinal magnetisation, M_{xy} is the component in the transverse plane
and θ is the nutation angle. At this point, the transverse magnetisation will precess around $\vec{B}_0$ with
the Larmor frequency.

2.1.2   Relaxation

Following the excitation, there is a loss of coherence and the magnetisation gradually goes back to
the steady-state $\vec{M}_0$. The transverse component decays generally exponentially to zero and the lon-
gitudinal magnetisation goes back towards the z axis, which is caused by the interaction of individual
magnetic moments with local magnetic fields on a molecular level. This interaction leads to loss
of coherence, dephasing the components of transverse magnetisation, named transverse relaxation.
These two effects are named transverse, T_2 (transverse relaxation time) or spin-spin relaxation and
longitudinal, T_1 or spin-lattice relaxation, respectively. The surrounding environment of the nuclear
spin called 'lattice' is constituted of molecules with thermal motion that generate random fluctuating
magnetic fields dominated by dipolar coupling between nuclei, giving rise to a spin-lattice interaction
that induces the longitudinal relaxation. Each spin goes through local magnetic fluctuations owing to
the magnetic moments of the neighbouring nuclei. A transition between the two spin states can only
occur when the transverse component of the resultant fluctuating field $\vec{B}_{fluct}$, i.e. perpendicular to
$\vec{B}_0$, oscillates with a frequency of ω_0. Thus, the nuclei dissipates the energy accumulated by the RF
pulse and fall back to the lower energy state aligned with $\vec{B}_0$. Moreover, the changes in the proportion
of spins in each spin state are reflected in $\vec{M}_z$. The longitudinal relaxation is then given by:

$$M_z(t) = M_0 \left(1 - e^{-\frac{t}{T_1}}\right) + M_z(0)e^{-\frac{t}{T_1}} = M_0 \left(1 - e^{-\frac{t}{T_1}}\right) \tag{2.10}$$

where $M_z = 0$ at $t = 0$, M_0 is the magnetisation corresponding to the steady-state and T_1 is
the characteristic time constant unique for each compound and its chemical environment. T_1 corres-
ponds to the time taken to return to M_0 as well as the time taken for the initial magnetisation of the
spins by $\vec{B}_0$. In fact, T_1 is highly $\vec{B}_0$ dependent and the stronger the external field, the longer the T_1.

The transverse relaxation process is directly related with the interactions between the excited
spins and ruled by alterations in entropy. The spins state transition induced during the longitudinal
relaxation is responsible for the loss of coherence of the detectable transverse magnetisation, contrib-
uting to the transverse relaxation. There is no loss of energy during this process, which is described
by the following Equation:

$$M_{xy}(t) = M_{xy}(0)e^{-\frac{t}{T_2}} \tag{2.11}$$

where T_2 is the characteristic time constant. $|\vec{M}(t)|$ can never be larger than M_0, hence $T_2 \leq T_1$. The transverse relaxation mechanism is combined with the effects of $\vec{B}_0$ inhomogeneities, resulting in a faster decay of the transverse magnetisation with a shorter characteristic time constant T_2^*, given by:

$$\frac{1}{T_2^*} = \frac{1}{T_2} + \frac{1}{T_{2,macro}} \tag{2.12}$$

The macroscopic inhomogeneities thus cause the spins to dephase faster due to localised regions of different field strength. As these inhomogeneities are not time-dependent with respect to NMR processes, it becomes possible to cancel them by using specific pulse sequences.

2.1.3 Bloch Equations

When a magnetic moment $\vec{\mu}$ feels the effect of a magnetic field $\vec{B}$, it experiences a torque proportional to the time derivative of the angular momentum (Graaf, 2007). Since the magnetisation is the sum of the individual magnetic moments, it becomes possible to extend the concept of motion for a single magnetic moment to the total magnetisation:

$$\frac{d\vec{M}(t)}{dt} = \vec{M}(t) \times \gamma \vec{B}(t) \tag{2.13}$$

where $\vec{B}(t)$ includes the static magnetic field $\vec{B}_0$ and time-varying components. At thermal equilibrium the total magnetisation corresponds to $\vec{M}_z$, which is perturbed by a RF magnetic field linearly polarized along the x axis with the corresponding expression in the laboratory frame:

$$\vec{B}_1(t) = 2B_{1,max} \cos \omega t \cdot \vec{e}_x \tag{2.14}$$

where $B_{1,max}$ is the maximum amplitude of the RF field, ω represents the angular frequency and $[\vec{e}_x]$ is a unit vector on the x axis. Decomposing it into two circularly polarized fields that rotate about the z axis in opposite directions:

$$\vec{B}_1(t) = B_{1,max}(\cos \omega t \cdot \vec{e}_x + \sin \omega t \cdot \vec{e}_y) + B_{1,max}(\cos \omega t \cdot \vec{e}_x - \sin \omega t \cdot \vec{e}_y) \tag{2.15}$$

The interaction with the spins by the counter rotating field, i.e. opposite sense compared to the magnetic moment, is negligible. Therefore, it can be ignored and the RF field is now given by:

$$\vec{B}_{1x}(t) = B_{1,max}(\cos \omega t \cdot \vec{e}_x - \sin \omega t \cdot \vec{e}_y) = \vec{B}_{1x} \cos \omega t + \vec{B}_{1y} \sin \omega t \tag{2.16}$$

The magnetisation under precession, excitation and relaxation can be described from Equation (2.13) expanded to the complete Bloch equations, in the laboratory frame (Bloch, 1946):

$$\frac{dM_x}{dt} = \gamma[M_y(t)B_0 - M_z(t)B_{1y}(t)] - \frac{M_x(t)}{T_2} \tag{2.17}$$

$$\frac{dM_y}{dt} = \gamma[-M_x(t)B_0 + M_z(t)B_{1x}(t)] - \frac{M_y(t)}{T_2} \tag{2.18}$$

$$\frac{dM_z}{dt} = \gamma[M_x(t)B_{1y}(t) - M_y(t)B_{1x}(t)] - \frac{(M_z(t) - M_0)}{T_1} \tag{2.19}$$

The relaxation of the different components of the magnetisation occurs in an exponential manner, in accordance with the respective characteristic time constants T_1 and T_2 for the components

parallel and perpendicular to $\vec{B}_0$, respectively. The fractions at the end of the Equations (2.17)-(2.19) with the corresponding characteristic time constants are related with the relaxation process. which are subtracted and have the corresponding time constant. On the other hand, considering a new set of Cartesian axes (x', y', z') rotating about $\vec{B}_0$ with the frequency ω of the applied $\vec{B}_1$ field, the dynamics of the macroscopic magnetisation can be described in the rotating frame:

$$\frac{dM'_x}{dt} = (\gamma B_0 - \omega)M'_y(t) - \gamma M'_z(t)B'_{1y} - \frac{M'_x(t)}{T_2} \tag{2.20}$$

$$\frac{dM'_y}{dt} = -(\gamma B_0 - \omega)M'_x(t) + \gamma M'_z(t)B'_{1x} - \frac{M'_y(t)}{T_2} \tag{2.21}$$

$$\frac{dM'_z}{dt} = \gamma[M'_x(t)B'_{1y} - M'_y(t)B'_{1x}] - \frac{(M'_z(t) - M_0)}{T_1} \tag{2.22}$$

where M'_x, M'_y and M'_z are the components of the magnetisation in the rotating frame and B'_{1x} and B'_{1y} definitions are used as specified in Equation (2.16). Both z and z' axis are collinear with the external field $\vec{B}_0$. The conversion to a different reference frame means changes on the magnetic field vectors, i.e. if the reference frame rotates with the frequency of $\vec{B}_1$, then $\vec{B}_1$ will appear static. Moreover, the precessional motion of the magnetisation has a reduced angular frequency $(\Delta\Omega = \gamma B_0 - \omega)$ relative to the remaining static field $\vec{B}'_0$ and goes around an effective field $\vec{B}'_e$, given by:

$$\vec{B}'_e = \vec{B}'_1 + \frac{(\gamma B_0 - \omega)}{\gamma} \cdot \vec{e}_z \tag{2.23}$$

When $\vec{B}_1$ is applied on-resonance (concept addressed in section 2.1.5), the magnetisation simply rotates around $\vec{B}'_1$. If the RF pulse is off-resonance, the effective field is tilted from the transverse plane as it has a component along z. This situation leads to a more complex rotation, since the magnetisation will precess about the effective field.

2.1.4   Signal Detection

The signal detection in NMR is based on the Faraday's law of induction, where the transverse component of the macroscopic magnetisation precessing around $\vec{B}_0$ at the Larmor frequency induces an electromotive force (emf) in a coil placed closed to the sample. The coil used as a receptor is the same used as a transmitter to generate the $\vec{B}_1$ field. The time-dependence of the emf is named Free Induction Decay (FID) and is proportional to the transverse magnetisation, which is given by the Bloch equations:

$$S(t) \propto M_{xy}(t) = M_0 sin(\theta)e^{-\frac{t}{T_2^*}}e^{i\omega_0 t + \phi} \tag{2.24}$$

where θ is the flip angle of the excitation pulse and φ is the phase of the magnetisation at $t = 0$. The signal amplitude has its maximum value when the magnetisation is completely tilted into the transverse plane (i.e. $\theta = 90°$). It oscillates at a frequency ω_0 and decays exponentially with a characteristic time T_2^*. The FID holds the information on the resonating nuclei and corresponds to a complex signal in the time domain, therefore, it is Fourier transformed into the frequency domain and named spectrum. The respective real and imaginary frequency-domain signals that form the spectrum $S(\omega)$ are given by:

$$R(\omega) = A(\omega)\cos\phi - D(\omega)\sin\phi \tag{2.25}$$

$$I(\omega) = A(\omega) \sin \phi + D(\omega) \cos \phi \tag{2.26}$$

where $A(\omega)$ and $D(\omega)$ characterize the absortion and dispersion components of a Lorentzian lineshape, respectively:

$$A(\omega) = \frac{M_0 T_2^*}{1 + (\omega_0 - \omega)^2 T_2^{*2}} \tag{2.27}$$

$$D(\omega) = \frac{M_0 (\omega_0 - \omega) T_2^{*2}}{1 + (\omega_0 - \omega)^2 T_2^{*2}} \tag{2.28}$$

The real component of $S(\omega)$ has a width at half height of $1/(\pi\, T_2^*)$ and its peak is centered at the resonance frequency of the nucleus. The area under the peak is related with $\vec{M}_0$ as well as with the proportion of nuclear spins in the region under study. Generally, there is a phase distortion in the spectrum due to the mixture of absorption and dispersion signals. Therefore, the spectrum undergoes a phase correction in order to obtain purely positive absorption lineshapes.

2.1.5 Radiofrequency Pulses

Radiofrequency (RF) pulses take a central place in NMR experiments and are defined by its excitation profile, given by its Fourier transform. They generate a signal through the excitation mechanism of the magnetisation and enable several other spin manipulations for different purposes, e.g. cancelling the water resonance in a ^{1}H MRS spectrum (further explained in section 2.3.2.3). The RF pulse design and its correct implementation can significantly improve the experiment and therefore specific RF pulses have been developed.

An RF pulse is applied on-resonance when the difference between the Larmor frequency ω_0 and the frequency of the $\vec{B}_1$ field can be neglected, i.e. $|\gamma \vec{B}_1| \gg |\Delta\Omega|$, where $\Delta\Omega$ is the frequency offset. Conventionally, the flip angle is given by:

$$\theta = \gamma \int_0^\tau B_1(t)\ dt \tag{2.29}$$

where τ is the duration of the pulse and $\gamma \cdot B_1(t)$ is the RF power sent into the coil. The pulse bandwidth is an important parameter since a large bandwidth excitation pulse is necessary to excite a broad range of resonance frequencies or a selective pulse to saturate specific resonances such as water. If one doubles the RF power or the duration of the pulse this will result in a twofold increase in the flip angle, but not in the frequency band selectivity or pulse bandwidth as this is inversely proportional to the pulse length. Thus, by setting a high transmitter power that enables short pulse lengths for a given flip angle, a wide bandwidth and uniform excitation are obtained.

There are several types of RF pulses used in NMR: square pulses with constant amplitude and short hard pulses that generate a nonselective excitation of the spins across a given frequency range; sinc and Gaussian pulses with selective frequency profiles that can be designed using Fourier transform theory, the Bloch equations or optimization procedures (Bernstein et al., 2004c); composite RF pulses, amplitude and frequency-modulated adiabatic RF pulses with minimized $\vec{B}_1$-dependence of the nutation angle, that help reducing artefacts and increase sensitivity (Graaf, 2007).

2.1.5.1   Adiabatic Pulses

NMR research have made major breakthroughs in the design of complex RF pulses in order to overcome changes in $\vec{B}_1$ amplitude and to increase bandwidths (Tannús and Garwood, 1997). Adiabatic Pulses (AP) are amplitude and frequency-modulated hard pulses that generally enable the greatest combined immunity to $\vec{B}_1$-inhomogeneities and resonance offsets, provided that the power is above a certain threshold value. In this conditions, spins can be excited with a uniform nutation angle regardless of different $\vec{B}_1$ fields along the sample, as it only depends on how the field varies the amplitude and frequency during the pulse.

The motion of the spins can be visualized best in the rotating frame $(\hat{x}, \hat{y}, \hat{z})$ as previously described, however, it is now precessing around $\vec{B}_0$ at the instantaneous frequency $\omega(t)$ of the pulse, and then is called frequency-modulated (FM) frame. In the FM frame, $\vec{B}_1(t)$ does not precess in the transverse plane and has a constant orientation (arbitrarily chosen along x, Figure 2.3). As
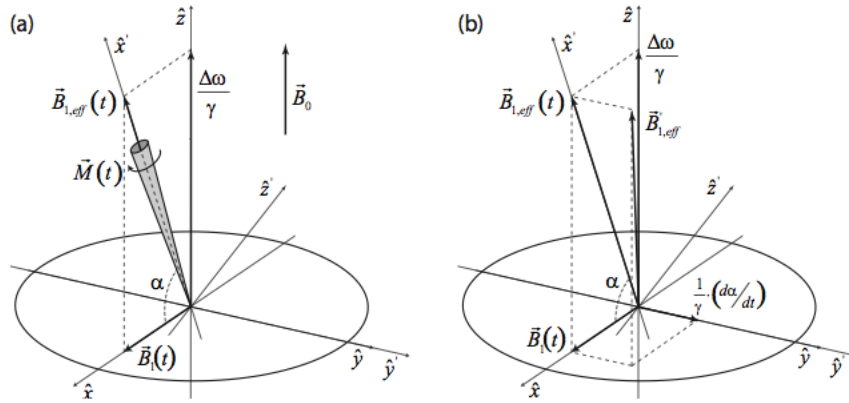
Figure 2.3: (a) The effective field $\vec{B}_{1,eff}(t)$ expressed in the frequency modulated frame. (b) The new effective field $\vec{B}'_{1,eff}(t)$ described in the second rotating frame $(\hat{x}', \hat{y}', \hat{z}')$ (Kunz, 2010).

AP are modulated pulses, the frequency of the pulse deviates from the Larmor frequency over time. Consequently, a longitudinal field arises changing the orientation of the effective field $\vec{B}_{1,eff}(t)$ towards the target flip angle. Its magnitude is given by:

$$B_{1,eff}(t) = \sqrt{B_1^2(t) + \left(\frac{\Delta\omega(t)}{\gamma}\right)^2} \qquad (2.30)$$

where $\Delta\omega(t) = \omega(t) - \omega_0$. Regarding the motion of the different fields, a better illustration is possible making use of a second frame $(\hat{x}', \hat{y}', \hat{z}')$ where x' is following the orientation of $\vec{B}_{1,eff}(t)$. The latter frame rotates around $\hat{y}$ (i.e. $\hat{y}' \equiv \hat{y}$) at the instantaneous angular velocity of $d\alpha(t)/dt$, where $\alpha(t)$ is given by:

$$\alpha(t) = \arctan\left(\frac{\Delta\omega(t)}{\gamma B_1(t)}\right) \qquad (2.31)$$

Therefore, a new effective field vector $\vec{B}'_{1,eff}(t)$ is formed with the given magnitude:

$$B'_{1,eff}(t) = \sqrt{B_{1,eff}^2 + \left(\frac{d\alpha(t)}{\gamma dt}\right)^2} \qquad (2.32)$$

There is an additional contribution of the angular velocity that makes the magnetisation vectors initially parallel with $\vec{B}_{1,eff}(t)$ to an incoherent precession around the $\vec{B}'_{1,eff}(t)$ instead, as a

function of frequency offset and RF amplitude. However, given that this contribution is substantially smaller than the amplitude of $\vec{B}_{1,eff}(t)$ it can be neglected and then $\vec{B}'_{1,eff}(t) \approx \vec{B}_{1,eff}(t)$. In order to meet this requirement, one can use sufficiently high $\vec{B}_1$ amplitudes or a slow frequency sweep. The aforementioned circumstances are known as adiabatic condition, described by:

$$\left| \frac{d\alpha(t)}{\gamma dt} \right| \ll \left| \vec{B}_{1,eff}(t) \right| \tag{2.33}$$

The AP can be divided in two groups: adiabatic full passage (AFP) and adiabatic half passage (AHP) pulses. In the AFP pulses (i.e. 180°excitation) t ranges from 0 to τ and result in a complete inversion of the magnetisation towards $-z$. On the other hand, AHP pulses (i.e. 90°excitation) vary from 0 to $\tau/2$ and $\vec{B}_{1,eff}$ rotates onto the transverse plane. Both types of AP have been very popular for *in vivo* surface coil experiments, in particular AHP that are most commonly used for proton and phosphorus NMR spectroscopy and help improving the experiments with a broad and homogeneous excitation. Another advantage of AP is that only one experimental calibration of the RF power is needed for each coil, since using a higher amplitude than the threshold value in future experiments will eliminate the need of subsequent calibrations.

2.1.6 Radiofrequency Probe

The radiofrequency probes (RF probe) used in NMR experiments have two key functions: transmission by creating an oscillating magnetic field $B_1(\vec{r}, t)$ in the xy-plane to excite the sample; reception when the probe detects the rotating magnetic field generated in the xy-plane by the excited sample. The RF probes can be divided in three main types: volume coil that surround the sample and generate a homogeneous magnetic field; surface coil formed by loops of wire, which are more sensitive to the magnetisation but have a restricted spatial sensitivity; array coil made of several surface coil functioning at the same time to increase the field of view.

Surface coil are often used with *in vivo* NMR spectroscopy. They can be placed adjacent to a larger object thereby providing a very high efficiency, however, the major drawback is the generation of an inhomogeneous RF field which decreases with distance from the coil. The frequency range used in NMR ($1 - 1000$ MHz) is low enough to consider the electromagnetic law for direct current fields. Therefore, considering the Biot and Savart's law:

$$\vec{B}_1(\vec{r}) = \frac{\mu_0}{4\pi} \oint I \frac{\vec{dl} \times \vec{r}}{\vec{r}^3} \tag{2.34}$$

where I is the current that generates the magnetic field $\vec{B}_1(\vec{r})$ at the position $\vec{r}$ and μ_0 is the permeability constant of vacuum ($4\pi \times 10^{-7}$ Tm/A). Thus, the magnetic field created by a simple loop coil and given by Equation (2.34) equals to:

$$\vec{B}_1(x) = \frac{\mu_0 I R^2}{2(R^2 + x^2)^{3/2}} \cdot \vec{e}_x \tag{2.35}$$

where I is the coil current, R is the radius, x corresponds to the distance from the centre of the coil and $\vec{B}_1(x)$ is the x-oriented field created by the surface coil. By increasing the radius of the coil it is possible to increase the penetration depth, however, this leads to a severe loss in the coil sensitivity.

2.1.6.1   Quadrature

After a 90° RF pulse, the transverse component of the magnetisation induces an EMF in the probe created by a magnetic flux going through the coil. A surface coil composed of a single loop C_1 and positioned orthogonal to the x-axis is not sensitive to the direction of rotation of the magnetic field and therefore performs only a linear detection, missing the phase information of the magnetisation vector. This issue can be addressed by adding a second coil C_2 perpendicular to the previous one, which experiences the same EMF now dephased of 90°. The full complex signal acquired in the quadrature setup has an overall improvement in the signal to noise ratio (SNR) by a factor of $\sqrt{2}$ (Chen et al., 1983). Additionally, this geometry enables a larger field of view as well as a better $\vec{B}_1$ homogeneity.

The geometry of the coil is of major importance to minimize the mutual inductance between the combination of coils described by the Faraday's law of inductance. Therefore, this coupling can be reduced by a design overlapping the two loops (Adriany and Gruetter, 1997).

2.2   Magnetic Resonance Imaging

Magnetic resonance imaging (MRI) is a noninvasive technique that can be used *in vivo* to assess structural and anatomical information regarding the distribution of different tissues within the sample under investigation, based on its NMR relaxation properties. By generating soft tissue contrast the technique is essential to know where to position the voxels used for MRS sequences and for shimming, creating optimal conditions for acquisition.

In order to construct an image, MRI techniques make use of linear magnetic field gradients for localization using a method called spatial encoding. There are three different approaches to localize the signal and spatially encode a 3D image data set: slice selection, frequency encoding and phase encoding. Several RF pulses and gradients are applied in sequence during a MRI acquisition and are usually described in a time diagram named pulse sequence.

2.2.1   Magnetic Field Gradients

The concept of MRI takes into account the resonance condition described by the Larmor Equation (2.5), which is used to obtain spatial information. In this case, the resonance frequency ω_0 is made position-dependent so that after Fourier transformation the different frequencies relate to their position rather than chemical shift, as described in section 2.3. This is accomplished by using another static magnetic field of which the amplitude varies linearly with the position, the so-called magnetic field gradients described by:

$$G_{\vec{r}} = \frac{dB_z}{d\vec{r}} \tag{2.36}$$

where $G_{\vec{r}}$ represents the gradients with x, y or z directions, given that $\vec{B}_0$ is always z-oriented. The direction of a gradient concerns to the direction in which the field strength varies (Fig. 2.4). Since the gradient adds to the external field on one side and subtracts on the other half of the magnet, the field strength of the gradients is null at the magnet's isocenter (Graaf, 2007). The total magnetic field at position $\vec{r}$ is then given by:

$$B_z(\vec{r}) = B_0 + \vec{G}_{\vec{r}} \cdot \vec{r} \tag{2.37}$$
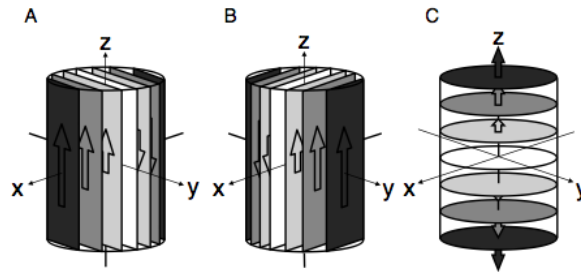
Figure 2.4: Gradients generate a magnetic field distribution in the x, y and z directions represented in A, B and C schemes, respectively. The relative amplitudes of the arrows indicate and the colour of the planes indicate the linear increase in the field strength as a function of position, such that in the white plane (i.e. middle of the gradient isocenter) the magnetic field strength is zero (Graaf, 2007).

2.2.2 Slice selection

The slice selection method consist of choosing a spatial slice of the object in the x-y plane by applying a magnetic field gradient in the z direction and a selective RF pulse, simultaneously. This combination creates a z position dependent range of frequencies ($\Delta\omega$) and a slice thickness determined by the gradient strength and the bandwidth of the RF pulse, according to:

$$G_z = \frac{\Delta\omega}{\gamma\Delta z} \qquad (2.38)$$

where Δz is the width of a certain slice of the object and $\Delta\omega$ is the bandwidth. Taken together, these parameters will define the slice, e.g. by increasing the gradient strength with unchanged bandwidth or decreasing the bandwidth with the same gradient strength will result in a narrower slice excitation (Fig. 2.5).
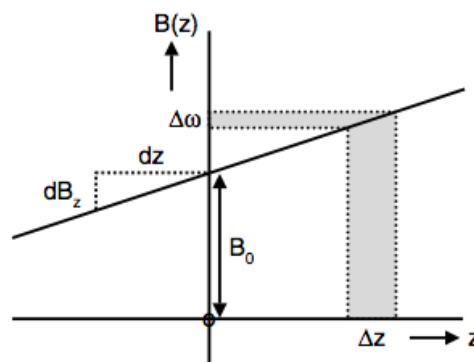
Figure 2.5: Principle of slice selection with a magnetic field gradient in the z direction. A selective range of frequencies corresponds to a selective range of spatial positions (i.e. slice) (Graaf, 2007).

2.2.3   Frequency encoding

After selecting the spatial slice, it has to be encoded in two dimensions that is one pixel in k-space (section 2.2.5) corresponds to a single spatial frequency. This is accomplished by applying two gradients to encode in the x and y directions at different times, so that they can be differentiated from one another.

Encoding in the x direction involves a first stage prior to acquisition where a constant gradient G_x is applied in one direction for a time t, to prepare the transverse magnetisation for encoding spatial information. Therefore, it is generated a position-dependent phase shift in the spins as described by the following equation:

$$\phi(x,t) = \gamma x G_x t \tag{2.39}$$

After the first gradient, the transverse magnetisation is encoded at each position x of the spins. In order to perform the signal acquisition, a second gradient of the same magnitude and opposite sign is applied for twice the time, such that the acquired phase shift equals zero in the middle of it. At that moment, the signal strength is maximal and an echo is formed. As the second gradient is applied during the period when the receiver components are turned on, it is called 'readout' gradient.

2.2.4   Phase encoding

The phase encoding gradient G_y is applied in the y-direction while the spins resonate at different frequencies. Its application occurs before the frequency gradient and encodes the rows of k-space. After G_y, the spins resonate again at their original frequency with the difference that they now have a position-dependent phase. By maintaining the order by which phase and frequency encoding gradients are applied relative to one another and making constant the magnitude of G_x while G_y is modified after each excitation pulse, it becomes possible to fill row after row of the k-space.

2.2.5   Spatial frequency space (k-space)

The raw data from the MRI acquisition is stored in a matrix based on the space covered by the phase and frequency encoding data, so-called k-space. It represents the spatial frequency information and undergoes a 2D Fourier transformation in order to create an image (Moratal et al., 2008). To obtain the optimum image is essential that the entire k-space is filled. The spatial frequencies k_{FE} and k_{PE} correspond to the x and y directions and are given by:

$$k_{FE} = \gamma G_{FE} \Delta t \tag{2.40}$$

$$k_{PE} = \gamma G_{PE} \tau \tag{2.41}$$

where G_{PE} and G_{FE} are the phase and frequency encoding gradients respectively, Δt is the sampling time and τ is the duration of the phase encoding gradient. The gradients strength and time taken for acquisition are parameters that can be adjusted in order to get the desired field of view (FOV). The coordinates close to the middle of k-space are named low spatial frequencies and contain signal to noise and contrast information. On the contrary, the outermost coordinates are referred to as high spatial frequencies and contain information on the image resolution. Thus, the quality and

clearness of images in MRI mainly depends on the following: signal to noise ratio (SNR), contrast between different tissues and spatial resolution (Gallagher et al., 2008).

2.2.6 Gradient echo

The gradient echo (GE) sequence begins with an RF pulse between 0 and 90° to excite the sample onto the transverse plane at the same time as a slice selective gradient is applied. Then, the phase encoding gradient is applied to encode a row of k-space. In order to dephase the spin isochromats (i.e. set of spins that resonate at the same frequency), an initial 'prephasing' gradient is applied in the frequency encoding direction followed by a rephasing readout gradient that has opposite polarity, same magnitude and twice the area. Therefore, the two gradients cancel each other creating a full echo halfway through the application of the second one, the so-called Gradient Echo. Each sequence ends with the application of a phase encoding rewinder lobe such that the spins return to their original state. Since several rows of k-space need to be encoded, the sequence would be repeated with different phase encoding gradients (Bernstein et al., 2004a).

The echo formation is influenced by several parameters: the longer the first phase encoding gradient, the longer will take for the echo to form; the smaller the flip angle, the shorter the T_1 recovery and hence the shorter the sequence will be. There may be loss of signal when using GE sequences as they are very sensitive to magnetic field inhomogeneities. This may cause the spin isochromats to dephase prior to the prephasing gradient resulting in a smaller ensemble of spins in phase when the echo is acquired. Additionally, the transverse relaxation in an inhomogeneous $\vec{B}_0$ field creates an echo with its amplitude exponentially attenuated with a time constant T_2^*. Therefore, considering the Equations (2.11) and (2.12):

$$M_{xy}(t) = M_{xy}(0)e^{-\frac{t}{T_2^*}} \tag{2.42}$$

The inhomogeneities create a variety of Larmor frequencies that makes the transverse magnetisation to relax faster with the T_2^* time constant instead of T_2. Since the used flip angles are small, T_1 effects are negligible.

2.2.7 Spin echo

The Spin Echo (SE) sequence is very similar to the GE one (Fig. 2.6) and makes use of the same initial sequence of encoding gradients, such that the major difference relies on the application of an additional 180° refocusing RF pulse. After a slice selective 90° RF pulse, the magnetisation is precessing in the xy-plane, while the spin isochromats are dephasing at different rates due to the T_2^* relaxation mechanism. Therefore, the signal is rapidly lost making any acquisition impossible. However, by applying a 180° inverting pulse halfway between the excitation pulse and the formation of the echo, the magnetisation vectors will rotate about y by 180° leading to a resetting of the the system's coherence. As the refocusing pulse is applied, both frequency encoding gradients have the same polarity. At this point, the spin echo is formed, there is no signal loss due to magnetic field inhomogeneities since the spins are back in phase and hence a separate contribution of T_2 is obtained. One possible way to measure the T_2 relaxation time using the spin echo sequence is to perform several experiments in which the echo time is varied. The corresponding spectra is given by:

$$M_{xy}(TE) = M_{xy}(0)e^{-\frac{TE}{T_2}} \tag{2.43}$$

where TE (echo time) is the time between the excitation pulse and the top of the spin echo,
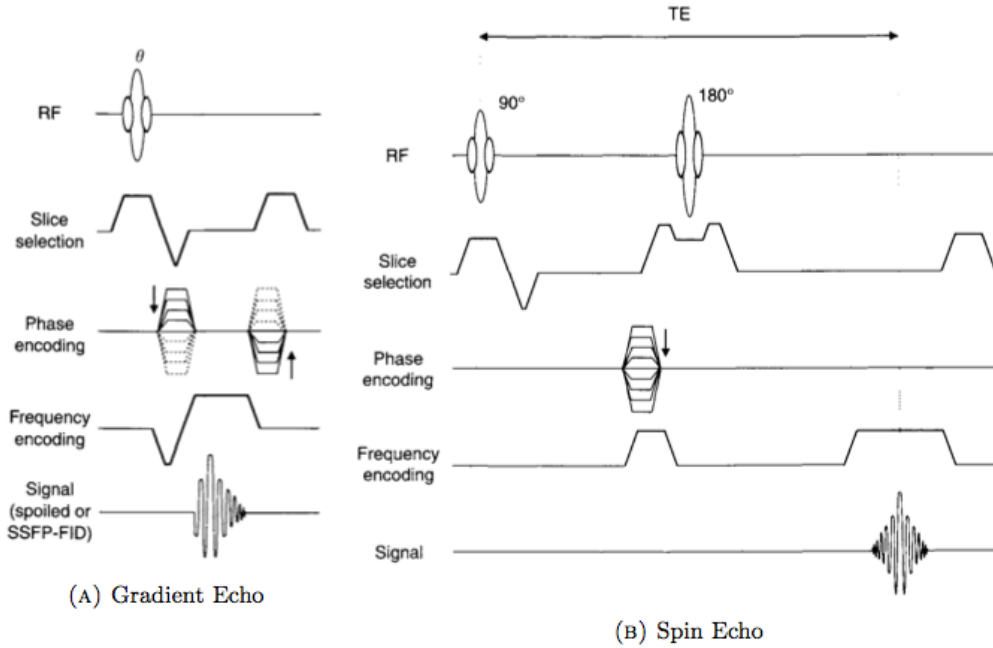
Figure 2.6: Gradient Echo sequence (A) as described in section 2.2.6 and Spin Echo sequence (B) as described in section 2.2.7 (Bernstein et al., 2004a).

where optimal refocusing occurs. The time between consecutive excitation pulses is referred to as repetition time (TR).

2.2.8   Rapid Acquisition with Rapid Enhancement (RARE)

The RARE sequence (Hennig et al., 1986) is a fast imaging sequence that makes use of a 90° excitation pulse followed by a series of 180° refocusing pulses to form multiple spin echoes. Each spin echo is separately spatially encoded and enables to acquire one line of k-space. Therefore, multiple lines can be sampled per excitation pulse thereby significantly reducing the scan time. The signal strength is proportional to the transverse magnetisation and decays according to:

$$S(n) = S_0 e^{-\frac{n t_{esp}}{T_2}} \tag{2.44}$$

where $S(n)$ is the echo signal, n is the echo index, $S(0)$ is the signal at $t = 0$ and t_{esp} is the time between echoes. The echo time of a RARE sequence is named effective echo time (T_{eff}) and is defined as the TE when the central k-space line is acquired. This type of sequence provides high image quality and less sensitivity to off-resonance effects (i.e. B_0 inhomogeneities and tissue magnetic susceptibility variations), being useful for clinical diagnosis (Bernstein et al., 2004b).

2.3   Magnetic Resonance Spectroscopy

In vivo MRS is considered a powerful tool that enables the study of cerebral metabolism non-invasively. Since disease may cause changes in metabolite concentrations, it becomes possible to quantify these

changes and monitor disease progression (Zwingmann, 2007). The main nuclei for MRS study are the following: proton (^{1}H), phosphorus (^{31}P), carbon-13 (^{13}C) and sodium (^{23}Na). It is required that the nucleus possess a magnetic moment (Mcphail et al., 2012). Since protons are present in nearly all metabolites, ^{1}H is the most commonly used for *in vivo* NMR spectroscopy among all nuclei, providing information over a large number of metabolites of mainly osmolytes, neurotransmitters and antioxidants.^{1}H MRS was performed in the experiments carried out in this report as well as ^{31}P MRS which allows to study the energy metabolism, intracellular pH and magnesium concentration.

2.3.1 Fundamentals of MRS

Since the proton nucleus has the highest sensitivity and high natural abundance, it generates the strongest NMR signal. Given that nuclei of the same element, or isotope, have the same gyromagnetic ratio, they would be expected to resonate at the same frequency when placed in the same external magnetic field B_0. However, the chemical environment of each nucleus is also affecting the resonance frequency (ω) and hence the position in the NMR spectrum. This phenomenon is referred to as the chemical shift (δ).The nucleus is surrounded by electrons that can be considered as small currents. This motion of charge generates a magnetic moment μ_e opposite to the external magnetic field. Thus, the magnetic field B sensed by the nucleus is reduced, which is referred to as electronic shielding, and alters the Larmor frequency and chemical shift. Therefore, the effective magnetic field B can be defined as:

$$B = B_0(1 - \sigma) \tag{2.45}$$

where σ is the screening constant, which depends on the chemical environment of the nucleus and is a dimensionless number.

The tendency of an atom to attract electrons towards itself is termed electronegativity. When a hydrogen atom is close to electronegative atoms the electron cloud is shifted away, thus reducing the electronic shielding and exposing the nucleus. Therefore, the Larmor frequency of that hydrogen nucleus will increase as well as the chemical shift. The latter is expressed as:

$$\delta = \frac{\nu - \nu_{ref}}{\nu_{ref}} \times 10^6 \tag{2.46}$$

where ν regards to the nucleus under investigation and ν_{ref} is the frequency of a reference compound. The chemical shift is expressed in ppm (parts per million) instead of Hertz, so that it is independent of the applied magnetic field and hence possible to compare directly the peak positions in spectra acquired among different NMR systems.

Besides chemical shift, another phenomenon takes place as a result of the chemical environment surrounding the nucleus. Either nuclei with a magnetic moment can interact directly through space (dipolar coupling) or indirectly through chemical bonds in the same molecule (spin-spin, scalar or J-coupling). In a liquid, the dipolar coupling is averaged to zero due to the fast molecular tumbling. However, the J-coupling do not average to zero and it can be described as a chain reaction between consecutive nuclear spins in a bonded network, propagated through the spins of the electrons present in the covalent bond. In the frequency domain spectrum, this gives rise to splitting patterns of the nuclear resonance into several peaks according to the number of energy level states of the covalently bounded nuclei. The gap between the peak defined by the scalar J, so-called nuclear coupling constant, is expressed in Hertz and gives information about the molecular structure and composition. Unlike chemical shift, it is independent of the external magnetic field B_0.

If one considers a molecule of two nuclei, A and B, with a nuclear spin $I = 1/2$ resonating
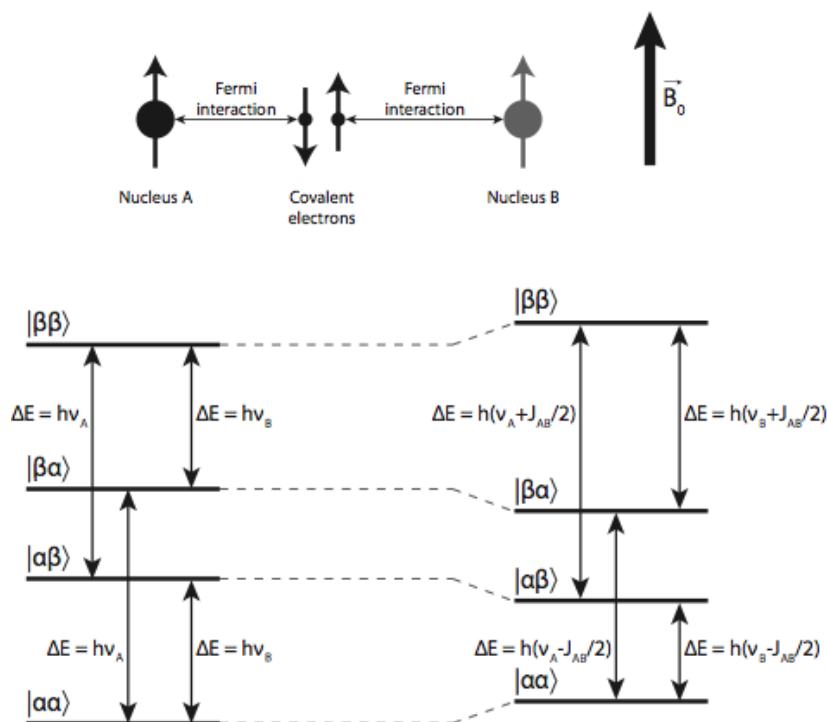
Figure 2.7: The Fermi interaction favours an antiparallel orientation between the nuclear and electronic spin and the Pauli exclusion principle forces the electron spins of the covalent bonds to be antiparallel. As the nuclear spins interact the energy levels of the system change, thereby resulting in different transition frequencies (Lanz, 2012).

at ν_A and ν_B, the electrons in this bond interact in accordance with the Pauli exclusion principle. Therefore, the electron spins have to be antiparallel. The nuclear spins, on the other hand, can be in any of the four possible combinations of their spin states: $\alpha\alpha$, $\alpha\beta$, $\beta\alpha$ and $\beta\beta$. If there is no bonding, the spectrum contains two lines (singlets) corresponding to the energy level transition of each nuclear spin, centred at their resonance frequency. When the nuclei are covalently bounded and taking into account the previously mentioned electron spin states, each nuclear transition is degenerated into two sub-levels depending on the coupling constant J_{AB}. Thus, the NMR spectrum now contains four lines with different frequencies. The new frequencies of the first and second pairs (doublets) are given by $\nu_A \pm J_{AB}$ and $\nu_B \pm J_{AB}$, respectively. In this case, the $\alpha\alpha$ and $\beta\beta$ are energetically less favourable states as one of the two bonding electrons is forced to be parallel to the nuclear spin, whereas in the other two states all spin orientations are allowed to be antiparallel.

The formation of the splitting pattern in the NMR spectra is related with the concepts of chemically and magnetically equivalent or nonequivalent nuclei. If two nuclei are chemically equivalent, they have the same chemical shift but distinct coupling constants when coupled to a third nucleus with different chemical shift. Magnetically equivalent nuclei have an identical coupling constant with the third nucleus. Overall, nuclei are equivalent if they have the same physical and chemical properties and there is no interaction between them and J-coupling effects. On the other hand, non-equivalent nuclei may give rise to complex splitting patterns explained by the method of successive splitting (Graaf, 2007). In this thesis, only weakly coupled spin systems are considered as they are the most

commonly found in ^{31}P *in vivo* NMR spectroscopy. This type of spin systems correspond to the so-called first-order NMR spectrum and hold the condition:

$$|\nu_A - \nu_B| \gg J_{AB} \qquad (2.47)$$

Take for instance the AMX spin system comprising three nonequivalent nuclei with fairly different resonance frequencies. Regarding A and X, each pattern is affected by M and splits into doublets in accordance with J_{AM} and J_{XM}, respectively. Since M is coupled to A and X, its pattern is split into four peaks of equal intensity, named a 'doublet-of-doublets'.

In general, the magnitudes of coupling constants are 1-15Hz for ^{1}H -^{1}H couplings, 10-20Hz for ^{1}H -^{31}P and 15-20Hz for ^{31}P - O -^{31}P. In the last case the coupling constant is for two bonds. The total area corresponding to all the multiplets of a certain resonance is proportional to the magnetization of the concerned nucleus and thus to its concentration.

2.3.2   Localization

For *in vivo* NMR spectroscopy is essential to have a well-defined region of interest (ROI). By using spatial localization it is possible to remove undesired signals from outside the ROI, thereby obtaining narrower spectral lines and more uniform signal excitation and reception. The localization techniques are mostly based on magnetic field gradients (section 2.2.1) and the application of a frequency-selective RF pulse. They can be divided in two categories: techniques that leave the magnetization in the selected 3D volume unperturbed and remove the unwanted external signal, hereafter referred to as outer volume suppression (OVS), e.g. avoid the contamination from extracranial lipids in MRS of the brain; techniques that selectively excite the magnetisation in the volume of interest (VOI), so that only that region generates signal.

2.3.2.1   Image Selected *In Vivo* Spectroscopy (ISIS)

The ISIS localization method first described in (Ordidge et al., 1986), makes use of three frequency-selective inversion pulses (180° RF pulses) and a 90° excitation pulse, as well as three orthogonal magnetic field gradients which intersection corresponds to the VOI. The inversion pulses are turned on and off. Two scans are needed to perform one-dimensional ISIS localization, whereas a full 3D localization needs eight successive scans in an addition-subtraction scheme, accumulating the desired signal and cancelling the signal outside the voxel. In order to obtain exact signal cancellation it is essential that tissue movement, e.g. breathing, is minimal. The main drawback of this method is the time taken to complete all the scans as well as the possibility of signal contamination for compounds with short T_2 relaxation times, which can be reduced by combining ISIS with OVS. In the present study, an ISIS module in the y-direction combined with OVS were used as well as signal excitation with an adiabatic RF pulse (further explained in Chapter 3).

Outer volume suppression is the successive excitation of slices placed around the VOI, using the more suitable gradient for the slice selection. The excited magnetisation is afterwards dephased using an additional gradient, so-called crusher. This process can be repeated for several slices around the VOI to avoid contamination from neighbouring regions.

2.3.2.2   Point Resolved Spectroscopy (PRESS)

The PRESS localization, often called double spin-echo method, is based on the combination of slice selective excitation with two refocusing pulses. Following the 90° excitation pulse and after a time t_1, the first 180° pulse is applied and creates a spin-echo at time $2t_1$. This spin-echo is then refocused by a second 180° pulse during a delay $2t_2$, such that the final spin-echo is formed at $TE = 2t_1 + 2t_2$, i.e. echo time of PRESS. The signal from the first echo comes from the intersection between the two orthogonal slices selected by the first excitation and refocusing pulses, whereas the second spin-echo contains the signal from the desired VOI (Graaf, 2007). Similar to ISIS, the VOI is defined at the intersection of the three selected slices, however, the three pulses are applied in a 'single-shot' acquisition and the signal is localized directly. Therefore, this makes PRESS less sensitive to movement-related outer-volume contamination than ISIS.

Another single-shot sequence is STEAM (Stimulated-Echo Acquisition Mode), which uses three orthogonal slice-selective 90° pulses in order to create a stimulated echo. The signal generated has half the SNR compared to PRESS. (B. Cady, 2012).

2.3.2.3 SPECIAL sequence

The SPECIAL (Spin Echo full Intensity Acquired Localised spectroscopy) sequence is a combination of one-dimensional ISIS localization (section 2.3.2.1) with a spin-echo acquisition (Mlynárik et al., 2006). It starts with a y-direction slice selective 2ms adiabatic 180° pulse. Then, a SE sequence performs slice selection in the x and z directions using 0.5ms and 1ms pulses, respectively. In accordance with the ISIS method previously described, the scans with the y-selective inversion pulses are added and the others subtracted. When performing MRS of the brain, OVS consisting of three modules of 1.2ms adiabatic pulses is used prior to the main sequence, in order to cancel undesired signal from lipid-rich areas close to the edge of the brain. Water suppression, designed to minimize sensitivity to B_1 inhomogeneity, is achieved using a series of 25ms asymmetric variable power RF pulses with optimized relaxation delays (VAPOR) interleaved with OVS, where the bandwidths are 270Hz and 35kHz, respectively. One way to improve the water suppression (WS) is to add a frequency-selective 15ms saturation pulse of 180Hz in between the first adiabatic 180° pulse and the SE modules.

By using this sequence in localized proton spectroscopy at high magnetic fields (7T, 9.4T, 14.1T) with good shimming and ultra-short echo times, an accurate detection and quantification of approximately 21 metabolites is possible. While the short TE helps minimizing the distortion of spectral multiplets due to J-coupling and loss of signal due to T_2 relaxation, the high magnetic field provides a better SNR and spectral resolution.

2.3.3 Proton (^{1}H) Spectroscopy

Proton NMR has a high sensitivity, i.e. high gyromagnetic ratio (Table 2.1), and high natural abundance (>99.9 %). This makes *in vivo* ^{1}H MRS a powerful technique to assess a large number of biologically relevant metabolites which contain protons. However, spectral resolution might be compromised as metabolite detection is difficult due to the larger magnitude of the water than low concentration of metabolites, signal contamination from extracranial lipids and heterogeneous magnetic field distributions. Therefore, spatial localization (section 2.3.2) and water suppression are very important prerequisites for significant *in vivo* ^{1}H MRS studies. At 9.4T the Larmor frequency of ^{1}H spins is 400.23 MHz.

Metabolites are present in multiple processes such as osmoregulation, neurotransmission, en-

Isotope	I	γ (MHz/T)	ω_0 at 9.4T(MHz)	Natural abundance (%)
^{1}H	$I = 1/2$	42.578	400.23	99.985
^{13}C	$I = 1/2$	10.708	100.66	1.07
^{31}P	$I = 1/2$	17.252	162.16	100
^{15}N	$I = 1/2$	4.3173	40.48	0.368

Table 2.1: Properties of the main nuclei studied by NMR (Kunz, 2010).

ergy metabolism and antioxidant metabolism. They are listed below according to their main cerebral function. The following chemical shifts are observed under ^{1}H MRS and are taken from literature (Govindaraju et al., 2000, Graaf, 2007).

2.3.3.1   Osmoregulation

Glutamine (Gln): It is primarily located in the astroglia and plays a key role in metabolism. Gln is synthesised from structurally similar Glu through Gln synthethase (GS) reaction. Its concentration increase significantly under hyperammonaemic conditions and it is thought to play an essential role in HE. Gln is observed as a triplet at 3.76 ppm and multiplets between 2.12 ppm and 2.46 ppm.

Total choline (tCho): It is mainly composed of phosphorylcholine (PC) and glycerophosphorylcholine (GPC) as well as traces of free choline. tCho behaves as an osmolyte in the brain and it is present in cell membranes. GPC has a singlet at 3.21 ppm and resonances at 4.31 and 3.66 ppm, whereas Choline contains a singlet at 4.31 ppm and multiplets between 3.5 and 4.3 ppm.

Taurine (Tau): It is involved in osmoregulation, neurotransmission modulation and it is present in all cells of the CNS. Its synthesis occurs in the liver and brain and its concentration decreases with age. It can be observed as two triplets centred at 3.25 and 3.42 ppm.

Myo-Inositol (Ins): Its proposed functions include kidney osmotic regulation and acts as a cerebral osmolyte, which has been found in different neuronal cell types. It has been shown that Ins concentration changes of cognitive impairment and brain injuries. It is observed at 3.52 ppm as a doublet-of-doublets and triplets at 3.61, 3.27 and 4.05 ppm.

2.3.3.2   Neurotransmission

Aspartate (Asp): It is a nonessential amino acid and excitatory neurotransmitter that does not cross the blood-brain barrier. It gives rise to three doublet-of-doublets at 3.89, 2.65 and 2.80 ppm.

Glutamate (Glu): It is a nonessential amino acid that plays a major role as a neurotransmitter and synthesis of other compounds. It is observed as a doublet-of-doublets at 3.75 ppm and several multiplets between 2.04 and 2.35 ppm.

2.3.3.3   Energy Metabolism

Alanine (Ala): It is a nonessential amino acid generated from muscle glycolysis together with α-ketoglutarate, prior to moving into the liver. There, the reverse reaction takes place and glucose is sent back to the blood stream. Ala plays a major role in the glucose-alanine cycle between liver and tissues and is also present in mammal brain following brain ischemia, i.e. deficient blood flow to the brain. It gives rise to a doublet and a quartet resonance at 1.47 ppm and 3.78 ppm, respectively.

Lactate (Lac): It is formed via anaerobic glycolysis and is thought to link the astroglial glucose metabolism and neuronal metabolism. Lac is found at low concentrations in healthy brain, however, it has been shown to increase in cases of impeded blood flow. It can be seen at 1.31 and 4.10 ppm as a doublet and a quartet, respectively.

Creatine (Cr) and Phosphocreatine (PCr): These two metabolites can be found in neuronal and glial cells and are crucial for tissue energy metabolism. Cr and PCr have a similar spectra with a methyl resonance at 3.027 and 3.029 ppm as well as a methylene resonance at 3.913 and 3.930 ppm, respectively. The methyl resonance peaks are too similar to be distinguished, whereas the methylene resonances can be separated at high magnetic fields ($> 7.0T$). As the concentration of total Creatine remains constant it is used as an internal concentration reference. Creatine also plays a role in cerebral osmoregulation.

2.3.3.4 Antioxidant Metabolism

Ascorbate (Asc): It is a water-soluble antioxidant, so-called Vitamin C, with high concentration levels in the brain in both neurons and astrocytes. Asc resonances can be observed as a doublet at 4.49 ppm and multiplets at 4.00 and 3.73 ppm.

Glutathione (GSH): It is mainly located in the astrocytes and it is responsible for maintaining red blood cell structure and providing an amino acid transport system. It gives rise to a singlet along with a doublet-of-doublets at 3.77 ppm, two multiplets at 2.15 and 2.55 ppm and three doublet-of doublets at 2.93, 2.98 and 4.56 ppm.

2.3.4 Phosphorus (^{31}P) Spectroscopy

Phosphorus NMR has relatively high sensitivity (about 7% of proton sensitivity) and a 100% natural abundance, which enables the acquisition to be performed within minutes. Moreover, phosphorus *in vivo* compounds have a fairly large ($\sim$30ppm) chemical shift dispersion providing good spectral resolution, even at low magnetic field strengths. At 9.4T the Larmor frequency of ^{31}P spins is 162.16 MHz. *In vivo* ^{31}P MRS is very useful to study energetic processes, as it provides information through the detection of all metabolites that play key roles in tissue energy metabolism.

2.3.4.1 Identification of Resonances

Unlike ^{1}H NMR, ^{31}P NMR spectra holds a restricted number of biologically relevant resonances summarized in Table 2.2, given that all chemical shifts are by convention referenced relative to phosphocreatine (PCr) set at 0.00 ppm. These resonances are sensitive to certain physiological parameters, such as intracellular pH and ionic strength (e.g. of magnesium). Therefore, the changes in the chemical shift rely on alterations in the chemical environment of the nuclei due to protonation (acidification) or formation of a complex ion of magnesium with a compound. As a result of this dependence, intracellular pH and magnesium concentration can be deduced from the chemical shifts of various ^{31}P metabolites of the observed spectra. The most commonly used is the resonance of inorganic phosphate (P_i) relative to PCr, since it is observed in most tissues and it has a large dependence on the pH (B. Cady, 2012). The resonance of PCr can be assumed constant in the physiological pH range.

Phosphorus spectra is also characterized by homonuclear scalar coupling for ATP and heteronuclear (^{31}P-^{1}H) scalar coupling for the phosphomonoesters (PME), phosphorylethanolamine and phosphorylcholine, and phosphodiesters (PDE), glycerol 3-phosphorylethanolamine and glycerol 3-phosphorylcholine. In the same manner as chemical shift, the scalar coupling constants are also sensitive to the pH and magnesium (Mg^{2+}) concentration.

Combining ^{1}H and ^{31}P MRS enables the study of several important metabolites. The spectroscopy technique requires ultra-short TE sequences and a high magnetic field strength, so that the metabolites can be well distinguished from the macromolecules and an optimum definition of the resonance peaks is obtained. In addition, ultra-short TEs reduce the J-coupling evolution effects and signal loss caused by T_2 relaxation.

Adenosine monophospate (AMP)		6.33
Adenosine diphosphate (ADP)	α	-7.05
	β	-3.09
Adenosine triphosphate (ATP)	α	-7.52
	β	-16.26
	γ	-2.48
Dihydroxyacetone phosphate		7.56
Fructose-6-phosphate		6.64
Glucose-1-phosphate		5.15
Glucose-6-phosphate		7.20
Glycerol-1-phosphate		7.02
Glycerol-3-phosphorylcholine		2.76
Glycerol-3-phosphorylethanolamine		3.20
Inorganic phosphate		5.02
Phosphocreatine		0.00
Phosphoenolpyruvate		2.06
Phosphorylcholine		5.88
Phosphorylethanolamine		6.78
Nicotinamide adenine dinucleotide (NADH)		-8.30

[†] All chemical shifts are referenced relative to phosphocreatine at 0.00 ppm.

Table 2.2: Chemical shifts of biologically relevant ^{31}P-containing metabolites (Graaf, 2007).

2.3.5 Biochemistry

In order to evaluate the physiological state of the test subjects blood plasma, urine and stool samples were taken and information regarding the following compounds was obtained.

Bilirubin: It is excreted in bile and urine and an indicator of certain diseases. In HE, an increase in bilirubin levels is associated with biliary cirrhosis and it is a good indicator whether the bile duct has been sufficiently obstructed.

Glucose: It is an important energy-delivering substrate in cellular metabolism used as a precursor and is metabolised in glycolysis. Glucose levels are a good indicator of hypoglycaemia in the presence of carbohydrate metabolism disorders.

Glutamic pyruvic transaminase (GPT) and Glutamic oxaloacetic transaminase (GOT): It is a good indicator of bile duct problems when demonstrating high levels and it is commonly related to hepatocellular injury.

2.3.6 Spectral Quantification

The main purpose of obtaining an MRS spectra is to be able to determine absolute concentrations of the metabolites afterwards. The concentration is directly related with the magnetisation in the voxel measured and hence the area under the peaks, used to the quantification of metabolites.

Generally, a quantification method makes use of a reference compound, which information was acquired under the same conditions as the metabolite spectrum. The most used reference compound in ^{1}H MRS is water, since its concentration in different parts of the body is well known. However, it is acquired separately to avoid its large resonance peak overlaps with other metabolites. For ^{31}P MRS, PCr is used as a reference and is part of the desired spectrum. Therefore, metabolite concentration is given by:

$$[M] = [R]\frac{S_M}{S_R}C_{MR} \tag{2.48}$$

where $[R]$ is the concentration of the reference compound, S_M and S_R are the detected signals from the metabolite and the reference compound, respectively. C_{MR} is a correction factor between the metabolite and the reference that considers T_1 and T_2 relaxation times, gyromagnetic ratio, magnetic susceptibility, spatial position relative to the coil, amongst others. Since it might not be easy to calculate a reliable correction factor, metabolites ratios can be an alternative to use, however, prior knowledge about the reference compound's concentration is necessary. Additionally, by using ultra-short TE, the signal loss due to T_2 is reduced as well as the effects of scalar coupling (Graaf, 2007).

In order to separate and quantify each individual signal, there are several algorithms. In the present thesis, two of them were used for the data from each type of spectroscopy. For ^{1}H MRS, all spectra were analysed with LCModel (Provencher, 2001). The LC Model (Provencher, 2001) is based on the idea that the MRS signal can be described as a linear combination of each separate compound previously measured, so-called 'basis-set'. For ^{31}P MRS, AMARES (Advanced Method for Accurate, Robust and Efficient Spectral Fitting) (Vanhamme et al., 2001) was used to calculate metabolite amplitudes in the time domain, with the Magnetic Resonance User Interface (jMRUI).

Chapter 3

Materials and Methods

3.1   Preparation of Animals for Research

All the procedures and animal experiments were undertaken according to the local and federal rules. Male Wistar rats (150 ± 9g) were used in the experiments and undergone Bile Duct Ligation operations. Firstly, the rat was anaesthetised with 4% isoflurane, after which it remained between 1.5% and 2.5% for the rest of the operation. Then, it was placed on its back with the tail towards the surgeon, showing the shaved and disinfected surgical area where two incisions of 2.5-3.0cm were made first through the skin and second through the abdominal muscle, in order to access to the bile duct. Subsequently, the bile duct was isolated and tied in three different places 5mm apart from each other, starting close to the liver. Finally, the bile duct was sectioned between the second and third ligation. At the end, absorbable sutures were used to close skin and muscle incisions. The purpose of this operation is to block the bile in the liver, thereby leading to cirrhosis. For the behavioral tests, these animals were compared with other sham-operated animals.

3.2   MRI and MRS

The first MRI and MRS scans took place before the BDL operation and are named scan 0. Three more scans were performed for each rat at 4, 6 and 8 weeks after surgery and therefore each rat is its own control at scan 0. The choice of these time points was made according to significant changes in metabolite concentrations observed in previous studies (section 1.3.2.2). Taken together the time course of the disease and life expectancy of BDL rats, the determined end point was 8 weeks. At this point, histology was carried out on fresh brains collected immediately after decapitation.

All the ^{1}H and ^{31}P MRS experiments were performed on a 9.4T MRI actively shielded (Varian/Magnex, Palo Alto, CA) with a horizontal bore diameter of 30 cm. The system had a maximum gradient strength of 400 mT/m, slew rate of 3000 mT/m/ms, a rise time of 130 μs to reach this maximum strength and approximately 3 kHz/cm^2 second-order shim strength. A new home made surface coil was built, tested and used for ^{1}H MRS, ^{31}P MRS and MRI. The home-built RF surface coil was used as transceiver coil, consisting two single geometrically decoupled 16 mm loops, with a

linearly polarised phosphorous coil. It was placed close to the rat brain filling its whole FOV. This proximity to the brain together with the high static magnetic field strength allow to obtain a high SNR.   Before starting each experiment it was necessary to prepare the rats and the plastic holders. A thermosensor and its battery were connected and placed together at one side of the holder, while a fibre optical cable made the communication between the thermosensor and a computer. In order to monitor respiration, an air pillow was taped in the middle of the holder and below the rat. The computer showed a visual display of the temperature and respiration statuses.

In order to minimize the stress, obtain better results by avoiding animal movement and for ethical purposes, each rat was initially placed in a closed plastic box connected to the anaesthesia source and administered with 4% isoflurane. During the experiment, it was kept between 1.5% and 2% depending on the respiration levels maintained between 60 and 70 breaths per minute. After being removed from the box, the rat was weighted and fixed in a stereotaxic system (i.e. a pair of ear bars and a bite-bar) in order to keep the brain motionless. A nose mask worn by the rat during the whole experiment enabled to attach the anaesthesia tube and keep it close to the nose. The rat's body temperature was measured rectally, annotated at the beginning and kept at 37.5 ± 1.0 °C afterwards, by wrapping a warm water tube around the rat and covering it with paper tissue. After this preparation, half of the holder was placed inside the magnet so that the coil would already feel the effect of the static magnetic field. At this point, the tuning and matching of the coil was performed towards the proton and phosphorus Larmor frequencies (see Table 2.1), considering the respective loops. The holder was then positioned and fixed with screws to avoid any changes in the positioning during the experiment.

It is known that isoflurane may influence cerebral metabolite concentration and it has been shown that it only affects lactate, which increases over time. This effect was taken into account when analysing the data. After quantification, the data was averaged over the number of rats. A comparison between the scans at 0 weeks to each of the others was made in order to statistically analyse the data and assess whether the differences among healthy scans were statistically significant (i.e. $p < 0.05$), by using a t-test. All data was shown as the mean $\pm$ standard deviation.

3.2.1   Gradient Echo sequence (GEMS)

In order to assess the position of the rat, an ultra-short Gradient Echo multi-slice (GEMS) sequence was used. It had a duration of approximately 6 seconds and it was applied in the three planes (i.e. axial, sagittal and coronal). If necessary, the rat was repositioned by rotating and/or changing the in depth position of the holder inside the magnet and the new position was verified. The parameters were as follows: TE/TR = 2.5/20 ms, FOV: 30×30 mm, acquisition matrix: 128×128, 3 slices, thickness = 1 mm, gap between slices = 1 mm, flip angle 20°.

3.2.2   Fast Spin Echo sequence (FSEMS)

In order to obtain an anatomical image of the rat's head, an FSEMS (RARE) T_2 weighted sequence was used (section 2.2.8 for more details on RARE). The generated image allows the correct positioning of the voxels for both shimming and the MRS experiments. The parameters were the following: T_{eff}/TR = 52/4000 ms, FOV: 23×23, acquisition matrix: 256×256, 15 slices, thickness = 1.0 mm, gap between slices = 0.2 mm, Echo train length (E_{TL}) = 8, Echo spacing (TE_{sp}) = 13 ms.

3.2.3 ^{1}H MRS

The SPECIAL sequence (section 2.3.2.3) was used for the ^{1}H MRS experiments. The signal was acquired in the hippocampus, which is associated with memory function. A voxel of $2.0 \times 2.8 \times 2.0$ mm^3 shown at Fig. 3.1 was placed in this brain region. A slightly bigger volume of $2.5 \times 3.2 \times 2.5$ mm^3 was previously used for shimming and centred at the same position as the one used for the acquisition. In order to minimise the effects of J-coupling and reduce signal loss due to T_2 relaxation, a short TE of 2.8 ms was used (Mlynárik et al., 2006), as well as a long TR of 4 s to reduce the effect of T_1 relaxation. Therefore, the quantification is more reliable since less corrections need to be made. Moreover, OVS was performed to avoid contamination from lipid-rich areas and WS eliminate the water signal.
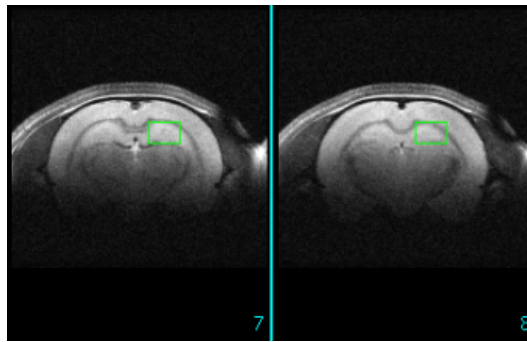

Figure 3.1: Screenshot illustrating the position of the voxel ($2.0 \times 2.8 \times 2.0$ mm^3) for ^{1}H MRS signal acquisition in the hippocampus.

Shimming was performed with the purpose of homogenise the $\vec{B}_0$ magnetic field in the desired VOI and was based on the Fast Automatic Shimming Technique by Mapping Along Projections (FASTMAP) (Gruetter, 1993). The shimming process can be divided into three stages. The first stage measures $\vec{B}_0$ along the x, y and z directions and a correction is made by the first order shim coil (x, y, z), whereas in the second stage the same happens but the field is measured along the xy, yx, xz, zx, yz, zy projections. The third stage is based on a version of FASTMAP (Gruetter and Tkac, 2000), where $\vec{B}_0$ is measured along the same directions as the second stage but the corrections are made by the second order shims (z^2, zx, zy, x^2-y^2, $2xy$). During this process, the shim coil's currents are changed after the measurements of $\vec{B}_0$ along the different projections. The goal is to make the water resonance as narrow as possible (i.e. decrease the linewidth of the water resonance), which is a reference of the field homogeneity. At the end of the shimming, linewidths ranging between 11 and 14 Hz were obtained given that the bigger the voxel, the more difficult is to reduce the water signal and thus higher linewidths arise.

In order to determine metabolite concentrations, linear combination modelling algorithms were used for quantification. The LC Model (Provencher, 2001) decomposes the *in vivo* spectrum by fitting its resonances into a linear combination of the individual metabolite spectral pattern measured *in vitro*, so-called 'basis-set'. This basis set was previously measured using aqueous solutions of all metabolites at the same temperature as that *in vivo* and using the same sequence parameters. The algorithms correct the frequencies, amplitudes, linewidths and phases of the basis set in order to find the best match to the acquired MRS signal. A ^{1}H MRS spectrum fitted by LC Model is shown at Fig.

3.2. For each metabolite concentration result, the lowest estimator-independent error is calculated and allows to quantify the reliability of each result. These are called the Cramer-Rao lower bounds (CRLB), described as followed: sufficient precision (CRLB < 10%), consider with caution (CRLB < 20-30%) and insufficient precision (CRLB > 30%). The resemblance between chemical structures among certain metabolites will give rise to higher lower bounds, since the CRLB increases with spectral overlap. In that sense, they should be only taken as a guideline. The metabolite concentrations are then determined using the areas under the peaks in the obtained spectra.

The scan with identical parameters but no water suppression was performed right after the MRS, thereby obtaining the water signal used as internal reference. It is known that water makes up 80% of the brain and has a concentration of 55Mol, therefore, absolute concentration is obtained by comparing the surface areas of the metabolite peaks with that of water. The acquisition was performed within a chemical shift ranging from 0 to 4.3 ppm and the following parameters: TE/TR = 28/4000 ms, voxel size $2.0 \times 2.8 \times 2.0$ mm^3, 160 averages.
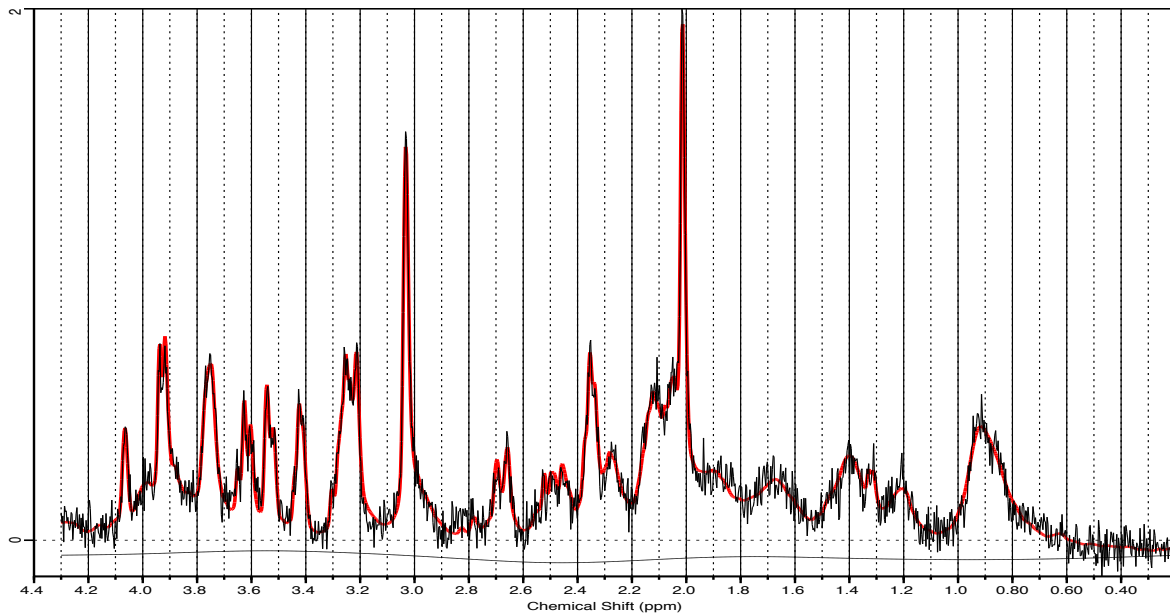
Figure 3.2: Screenshot of a ^{1}H MRS spectrum acquired in the hippocampus of a rat before BDL (scan 0) and fitted by LC Model. The red line represents the fitted spectrum and the black line is the measured spectrum. Parameters: TE/TR = 28/4000 ms, voxel size $2.0 \times 2.8 \times 2.0$ mm^3

3.2.4 ^{31}P MRS

For the ^{31}P MRS, the ^{1}H coil was replaced by the ^{1}H/^{31}P one. The shimming and imaging were performed using the proton loop and the spectroscopy using the phosphorous loop. Outer volume suppression (OVS) with 2.5 ms hyperbolic secant pulses was used for localization in x and z-direction as well as an additional one dimensional ISIS, in the y-direction, to reduce the contamination from the cheek muscles of the rat that affect the ^{31}P signal. The excitation was performed afterwards using a 1 ms broadband non-selective adiabatic half passage pulse (Mlynarik et al., 2012). A VOI of $4 \times 7.5 \times 6.5$ mm^3 resulted in linewidths between 17 and 20Hz using the following parameters: TR = 5000 ms, 6×64 averages, 2 dummy scans.

Shimming was performed using FASTMAP (Gruetter, 1993, Gruetter and Tkac, 2000) before the main sequence as in proton spectroscopy, in a voxel of $4.5 \times 8 \times 7$ mm^3 slightly bigger than the VOI. The jMRUI software was used to process the phosphorous spectra before the quantification.

After selection of the resonances and estimation of the chemical shift displacement for quantification, the AMARES program fits Lorentzian lineshapes to each peak in the time domain. Then it makes use of the first point of the FID (equivalent in the frequency domain to the surface area of the peak) to determine the relating amplitude and calculates the surface areas of each peak by integration, as shown in Fig. 3.3. It is possible to consider prior knowledge in AMARES, by introducing several parameters, such as amplitudes, linewidths and soft constraints on the chemical shift displacements.

For this study, the following resonances were considered: PE, PC, Pi, GPC, PCr, γ-ATP, α-ATP, NADP, β-ATP. A previous selection of resonances and estimation of linewidths was used as prior knowledge for the quantification and was slightly adjusted as needed. The metabolites concentration was expressed as a ratio referenced to PCr, shown to be stable in the ^{1}H MRS studies. Therefore, results were given as relative amplitudes.

3.3   Behavioral Tests

At week 6 and week 8 after surgery, behavioral tests were executed during the morning. For this purpose it was used a black arena with 100cm diameter and boundaries defined as follows: inner part with a 12.5cm radius from the centre, intermediate part with 37.5cm radius from the centre and outer part. The inner part was illuminated with 7-9 lux and the light was adjusted in order to have approximately 2 lux less in the outer part. The arena was cleaned with 5% ethanol and dried before each test. The experiment was recorded through a hardware-based realtime MPEG-2 (Moving Picture Experts Group-2) encoder secured to the ceiling above the centre of the arena, and a frame-grabber software (MediaCruise, Canopus Corporation, San Jose, CA, USA).

The test included two parts: the Open Field (OF) and the Novel Object (NO) tasks. For the first part, each rat was placed in the empty arena during 10 minutes. This was followed by the second part when a cylindrical object was placed in the centre during 5 minutes. The main purpose was to obtain the distance moved and the time under movement and immobile thereby analysing locomotor activity, as well as the time spent in the inner, intermediate and outer parts in order to assess the anxiety status.

3.4   Biochemistry

The blood from the rats was analysed longitudinally. Blood samples were taken from the tail vein, Bilirubin and Glucose levels were analysed. Plasma was collected after centrifugation for later analysis. All the remaining BDL rats were put asleep under anaesthesia and decapitated after 8 weeks. Their brains were collected according to the following procedure: the cranium was first removed and sliced into half. One half was kept in a mixture of formalin and then frozen for later histological studies. The other half was divided in parts (cerebellum, cortex, striatum and hippocampus) and kept in separate eppendorfs for wet/dry measurements for 4 days for assessing the water amount in the brain.
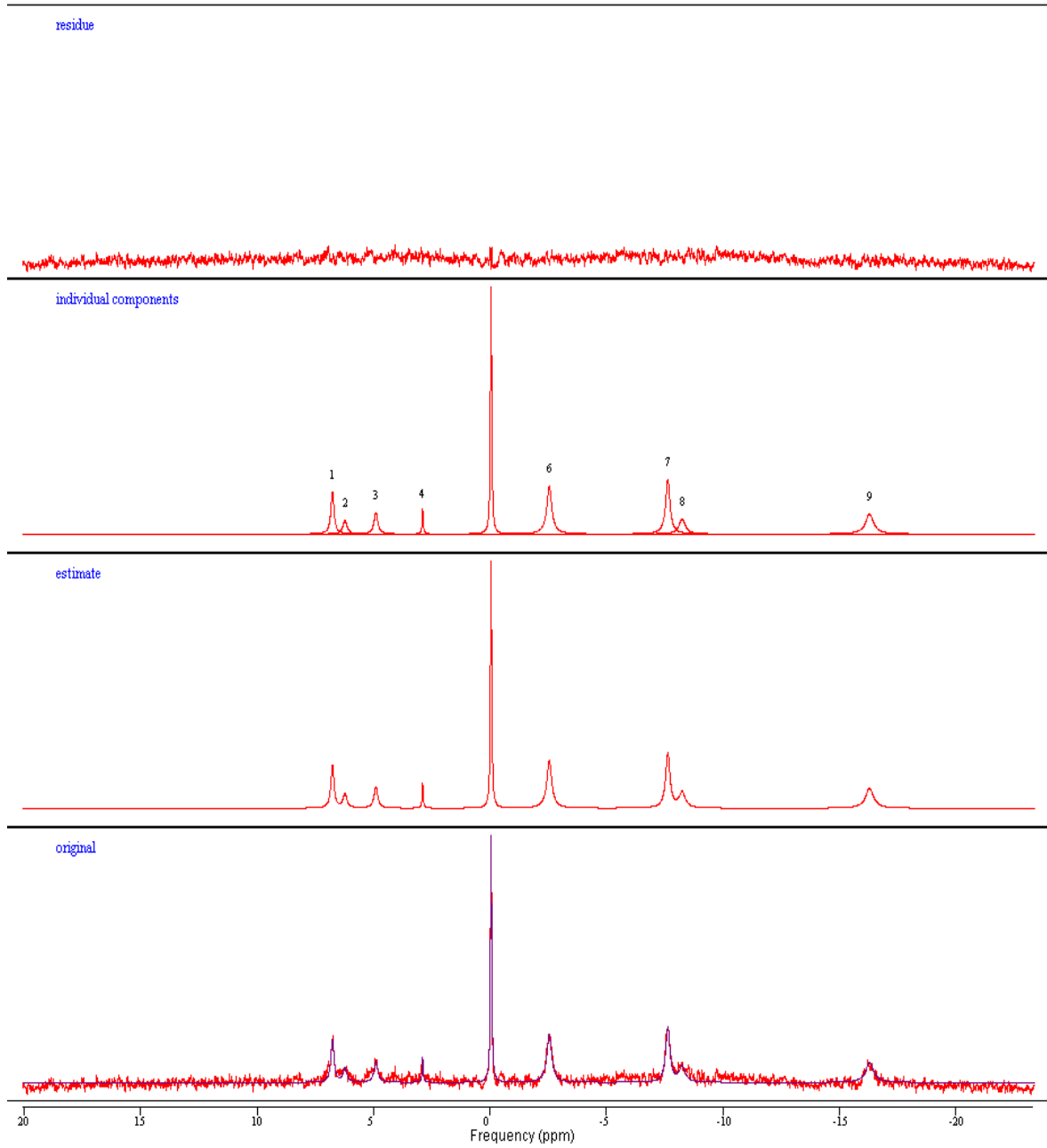
Figure 3.3: AMARES quantification. The measured signal shown in red is separated into individual components and then it estimates the amplitudes. This is shown by the blue line fitted to the acquired spectrum. The resonance peaks are labelled accordingly: 1 (PE), 2 (PC), 3 (Pi), 4 (GPC), 5 (PCr), 6 (γ-ATP), 7 (α-ATP), 8 (NADP), 9 (β-ATP).

Chapter 4

Results

The overall duration of a scan per rat considering animal preparation, ^{1}H MRS and ^{31}P MRS was approximately 3 hours. Therefore 5 rats were scanned for each time point among the 2 series of rats with a total of 10 rats for this study. All the ^{1}H MRS data obtained during this project will be incorporated into the data previously obtained at CIBM, by Dr. Cristina Cudalbu. To the best of our knowledge no in vivo ^{31}P MRS studies have been done with chronic HE BDL rat models except the preliminary results obtained in the laboratory by Arjun Jayaswal and Dr. Cristina Cudalbu. Concerning the behavioral tests they were executed by the author and the quantification done by Veronika Rackayová PhD.

4.1   Biochemistry

Bilirubin values were determined for all the rats before and after BDL surgery. Before BDL the levels were < 0.5 mg/dl and after BDL were 6-8 mg/dl showing levels above the threshold associated with liver disease. The measurements were performed longitudinally to ensure that the surgery was properly done and there was no recovery from the bile duct ligation.

4.2 ^{1}H MRS Data

The accurate detection of the 21 metabolites relied on a sufficiently high SNR for the ^{1}H MRS acquisition. As the severity of the disease increases so does the linewidth, making shimming more difficult. Therefore, the SNR decreased in the time frame of study as shown in table 4.1. The SNR was estimated by LC Model as the ratio of the maximum in the spectrum minus baseline over the analysis window to twice the root mean square residuals.

Time frame	Week 0	Week 4	Week 6	Week 8
Average SNR	22.7	22.2	18.6	20.0

Table 4.1: Average Signal to Noise ratio over time of the study.

4.2.1 Osmolytes

Gln: The average concentration at the beginning of the experiment (scan 0) was 3.4μ/g/tissue. This increased by 35% at week 4 (p=0.0046) and significantly increased by week 8 (136%) considering the initial concentration (p=0.0008). Additionally, was observed an increase of 42% at week 6. The mean standard deviation as a percentage for each week's average was around 25%. The CRLBs (the quantification errors) ranged between 3% and 9% with a mean value of 6%.

Ins: An overall decrease of 26% of the concentration level was observed (p=0.0003). There was a decrease below statistical significance from week 0 to week 6 of 2% (p=0.5), therefore, it only became statistically significant from week 6 onwards. The mean standard deviation was around 11%. The CRLBs ranged between 2% and 6% with a mean value of 4%.

tCho: An overall decrease of 4% was observed but not statistically significant (p=0.7). An initial insignificant decrease on the concentration level until week 4 was detected, it remained constant until week 6 and decrease afterwards until week 8 (insignificant). The mean standard deviation was around 18%. The CRLBs ranged between 7% and 29% with a mean value of 11%.

Tau: An overall decrease in concentration of 4% was observed below statistical significance (p=0.1). The concentration level remained constant until week 4 from where it started to decrease (insignificant). The mean standard deviation was around 6%. The CRLBs ranged between 3% and 5% with a mean value of 4%.

Cr: An overall decrease of 6% was observed, however, this was below statistical significance (p=0.09).There was a decrease in the concentration until week 4 of 3% also statistically insignificant. The mean standard deviation was around 7%. The CRLBs ranged between 4% and 9% with a mean value of 6%.

The total osmolyte concentration (Gln, Ins, Tau, Cr, tCho) was checked over the time frame of the experiment and it was found to remain approximately constant.

4.2.2 Neurotransmitters

Asp: A trend of decrease in concentration was observed from week 4 onwards as it remained constant (insignificant) until that moment. There was a sharp decrease from week 4 to week 6 of 27% of the initial concentration, statistically significant (p=0.0232). Despite the sharp decrease until week 6, an overall decrease of 8% was observed at scan 8, below statistical significance. Most of the CRLBs of all scans from week 6 onwards increased above the threshold of 20%, thereby making the results difficult to evaluate. The mean standard deviation was around 27%. A possible solution to verify these results will be increasing the number of animals under study.

Glu: An overall small decrease 4% was observed but not statistically significant (p=0.346), however, this decrease was not constant over the entire experiment and for the average concentration different trends were observed. The mean standard deviation was around 7%. The CRLBs ranged between 2% and 4% with a mean value of 3%.

4.2.3   Antioxidants

Asc (Vitamin C): An overall decrease of 11% in Asc concentration was observed by week 8, below statistical significance (p=0.138). The decreasing trend was constant over the experiment with 5% and 8% by week 4 and week 8, below statistical significance. The CRLBs ranged between 8% and 18% with a mean value of 13%. The mean standard deviation was around 13%.

GSH: A decrease of 17% was observed below statistical significance. However, the reliability of the data was poor and therefore cannot be taken into account. The CRLBs, excluding the null measured concentration ones, ranged between 14% and 58% with a mean value of 30%. The mean standard deviation was around 42%.

4.2.4   Energy metabolites

PCr: An overall decrease of 7% in the concentration levels was observed to be statistically insignificant (p=0.131). Small fluctuations were observed, an increase was observed until week 4 and started to decrease from that moment on. The mean standard deviation was around 8%. The CRLBs ranged between 3% and 8% with a mean value of 6%.

Ala: A trend of decrease was observed with an overall difference of 46% in the concentration level statistically significant (p=0.0489). However, in this case the data is not reliable, as one can see by the large mean standard deviation value (53%), due to the severe differences in the absolute concentrations of different rats. Additionally, the CRLBs ranged between 11% and 374% with a mean value of 48%.

Lac: An overall increase of 22% after 8 weeks was observed. This result was found statistically insignificant (p=0.291). There were fluctuations over disease progression: there was a decrease until week 4, followed by an insignificant increase until week 6 and continuing to increase over time. The mean standard deviation was around 34%. The CRLBs ranged between 7% and 29% with a mean value of 16%. Therefore, this trend of increase cannot be considered to be reliable.

Glc: An overall decrease of 77% was observed and statistically significant (p=0.0013). However, this is not reliable as the CRLBs ranged between 19% and 227% with a mean value of 52%. The mean standard deviation was around 68%. This trend was in accordance with the body blood glucose concentration levels from the blood samples.

The change in metabolite concentration over the progression of disease is shown in Fig. 4.1.
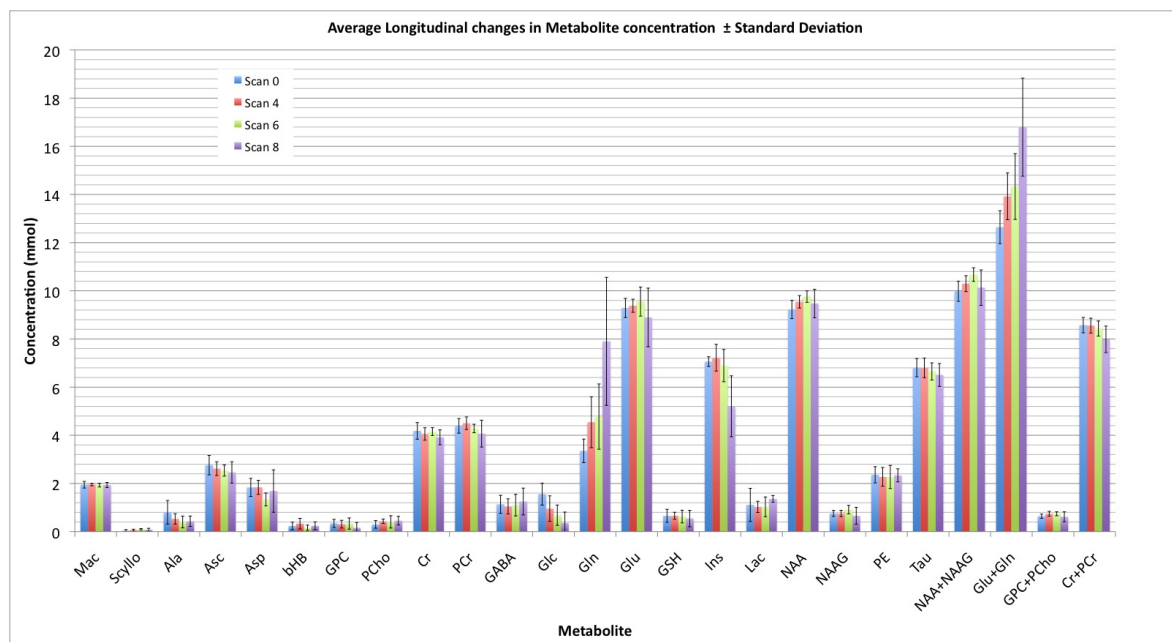
Figure 4.1: Average (n=10) longitudinal change in ^{1}H MRS metabolite concentration $\pm$ standard deviation error bars.

4.3 ^{31}P MRS Data

The spectra achieved were of good quality as shown in Fig. 4.2.. The linewidth considered acceptable for the chosen spectra was between 17Hz and 20Hz after shimming. Like this, the accurate detection of 9 metabolites relevant to energy metabolism was possible.
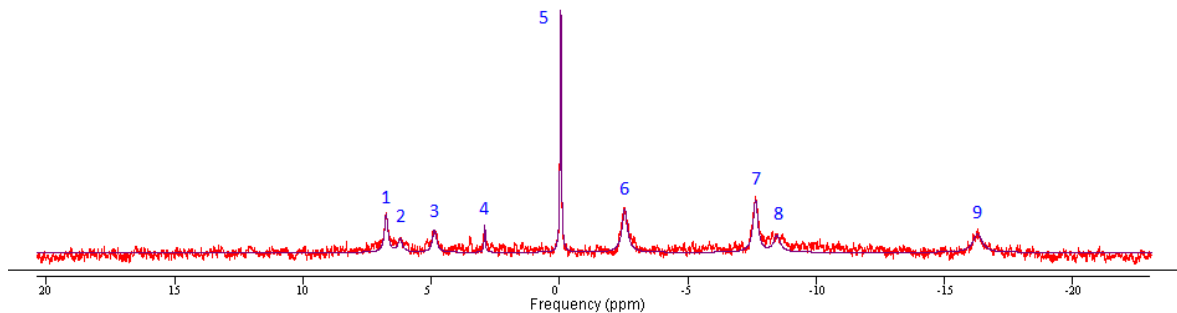

Figure 4.2: A ^{31}P MRS spectrum acquired in the hippocampus (voxel size $4 \times 7.5 \times 6.5$ mm^3, 6×64 averages). The resonance peaks are labelled accordingly: (1) PE, (2) PC, (3) Pi, (4) GPC, (5) PCr, (6) γ-ATP, (7) α-ATP, (8) NADP, (9) β-ATP.

Quantification of the ^{31}P MRS data was performed using AMARES. First of all, there was the input of prior knowledge on certain resonances. Regarding the linewidths, soft constraints on all resonances except PCr which was left to be estimated. In what concerns to chemical shift, Pi and PCr were left to be estimated and soft constraints applied on γ-ATP, β-ATP, α-ATP and PME. Regarding the amplitudes, they were all estimated. In what concerns to the phase of each resonance peak, all were set as 0.0 with no difference between them. After this approach, the chemical shift was slightly fitted for each signal if needed. Moreover, the resonances observed were referenced to PCr, since it has shown the most stable levels of concentrations in BDL rat studies performed at CIBM/LIFMET.

An overall trend of decrease was observed in γ-ATP of 9% difference in concentration at week 8, statistically significant (p=0.0180). A decrease trend was observed in α-ATP, β-ATP and PC statistically insignificant. A decrease of 25% statistically significant (p=0.03201) was observed in GPC at week 8. An overall decreasing trend was shown for PE, reaching statistical significance with a difference of 14% at week 6 (p=0.0234) and 20% at week 8 (p=0.0016). Both Pi and NADP showed an overall trend of decreasing statistically insignificant and were not constant since there were some fluctuations over disease progression. Nevertheless, was observed a statistical significant decrease in concentration levels of 11% in Pi at week 4 (p=0.0321).

In general, all metabolite concentration levels decreased over disease progression. The change in metabolite concentration is shown in Fig. 4.3.

4.4 Behavioral Tests

Behavioral tests (Open Field and Novel Object tasks) were executed the day before the respective scans at week 6 and week 8 after BDL surgery. For this purpose, BDL rats were compared with shams. The BDL rats had behavioral tests performed twice (weeks 6 and 8) and shams three times (weeks 4, 6 and 8). Therefore, in order to cancel the learning effect, weeks 6 and 8 of BDL rats were compared
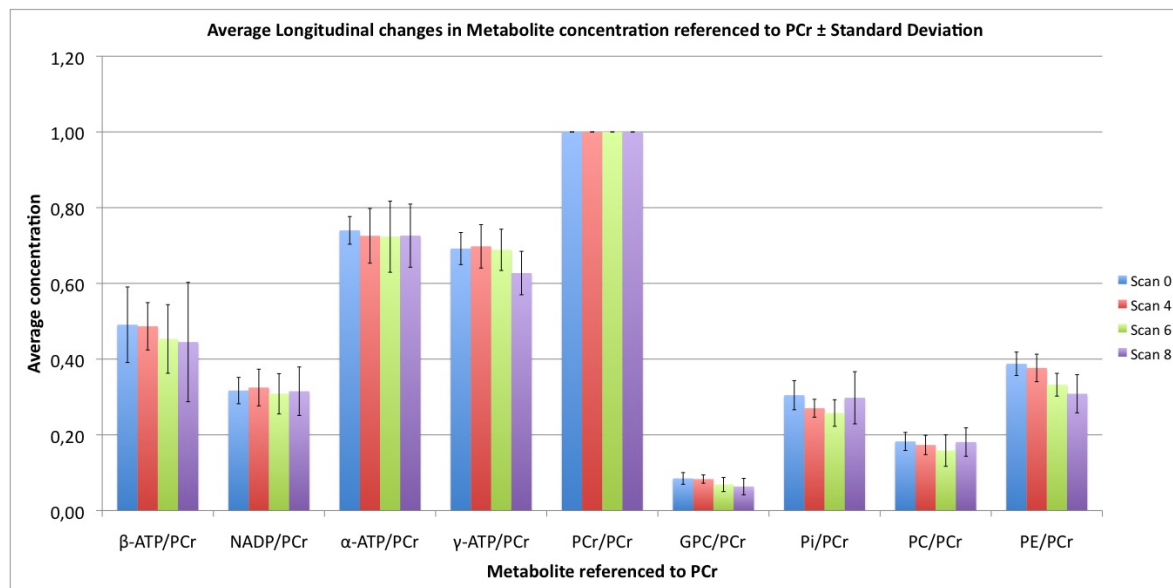
Figure 4.3: Average (n=10) longitudinal change in ^{31}P MRS metabolite concentration referenced to PCr ± standard deviation error bars.

with weeks 4 and 6 of shams, respectively.

4.4.1   Open Field Task

Concerning the OF task, the results obtained are shown considering the distance moved, the time spent under movement and immobile as well as the percentage of time spent in each region of the arena, comparing the population of BDL and sham-operated groups of animals.

The distance moved during the open field task at two different time points is shown in Figure 4.4. The BDL group presented a statistically significant lower distance moved in comparison with sham-operated group, at the first (p=0.0009) and second time point (p=0.0011).

The time spent under movement and immobile during the open field task at two different time points is shown in Figure 4.5. The BDL group spent statistically significant less time under movement and therefore more time immobile at the first (p=0.04) and second time points (p=0.0088) in comparison with the sham-operated group.

The percentage of time spent in the (a) inner, (b) intermediate and (c) outer parts of the arena during the open field task at two different time points is shown in Figure 4.6. It was observed in the BDL group a statistically insignificant lower time spent in the inner part of the arena and a statistically significant (p=0.0199) higher percentage of time spent in the outer part in comparison with the sham-operated group, at the second time point.

Figure 4.4: Distance moved during the open field task at two different time points. At the first time point, the BDL group (n=10) was compared with the sham-operated group (n=6). At the second time point, the BDL group (n=5) was compared with the sham-operated group (n=4). The differences were statistically significant.

<div align="center">(a)</div>

<div align="center">(b)</div>
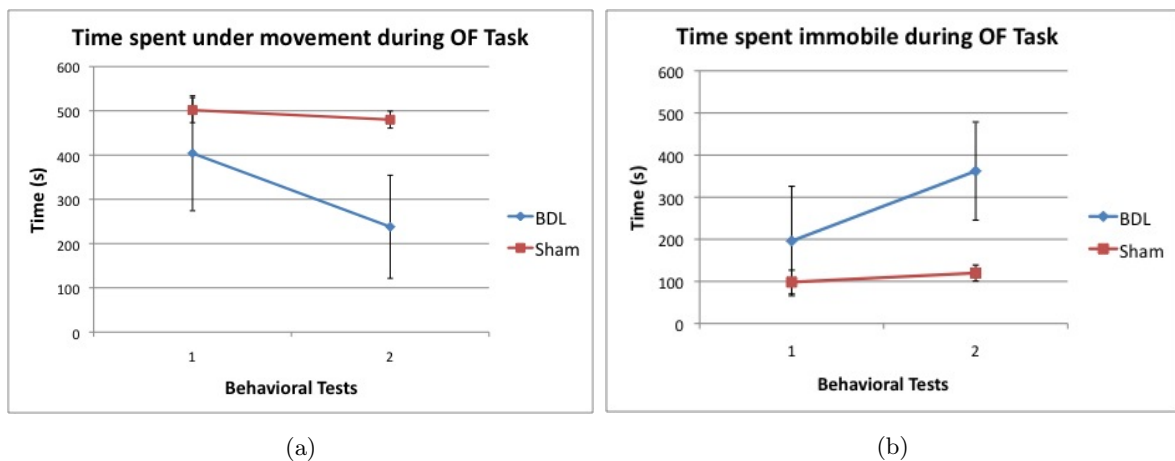
Figure 4.5: Time spent under movement (a) and immobile (b) during the open field task at two different time points. At the first time point, the BDL group (n=10) was compared with the sham-operated group (n=6). At the second time point, the BDL group (n=5) was compared with the sham-operated group (n=4). The differences were statistically significant.

(a)

(b)

(c)

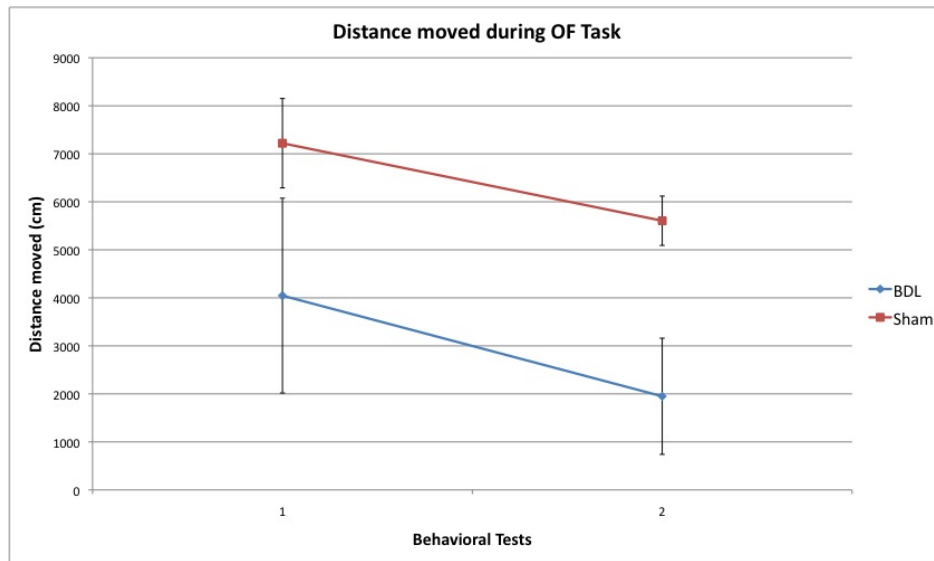Figure 4.6: Percentage of time spent in the (a) inner, (b) intermediate and (c) outer parts of the arena during the open field task at two different time points. At the first time point, the BDL group (n=10) was compared with the sham-operated group (n=6). At the second time point, the BDL group (n=5) was compared with the sham-operated group (n=4). The differences were statistically significant in situation (c).

4.4.2 Novel Object Task

Concerning the NO task and similarly to the OF previously analysed, the results obtained are shown considering the distance moved, the time spent under movement and immobile as well as the percentage of time spent in each region of the arena, comparing the population of BDL and sham-operated groups of animals.

The distance moved during the novel object task at two different time points is shown in Figure 4.7. The BDL group presented a statistically significant lower distance moved in comparison with sham-operated group, at the first (p=0.0371) and second time point (p=0.0018).

The time spent under movement and immobile during the novel object task at two different time points is shown in Figure 4.8. The BDL group spent less time under movement and therefore more time immobile at the first (insignificant) and second time points (statistically significant, p=0.0021) in comparison with the sham-operated group.

The percentage of time spent in the (a) inner, (b) intermediate and (c) outer parts of the arena during the novel object task at two different time points is shown in Figure 4.9. It was observed in the BDL group a lower time spent in the inner part of the arena and a higher percentage of time spent in the outer part in comparison with the sham-operated group, at the second time point. However, the results obtained were not statistically significant.
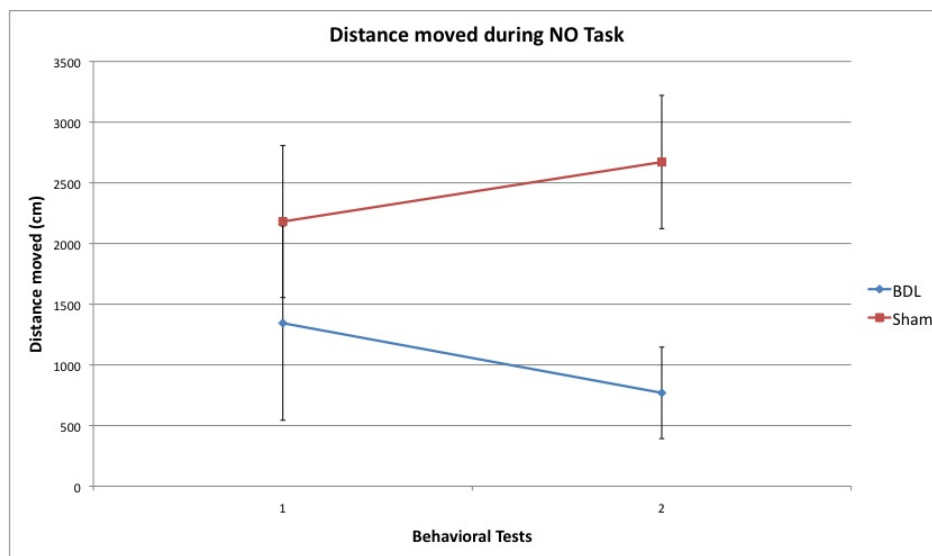
Figure 4.7: Distance moved during the novel object task at two different time points. At the first time point, the BDL group (n=10) was compared with the sham-operated group (n=6). At the second time point, the BDL group (n=5) was compared with the sham-operated group (n=4). The differences were statistically significant.
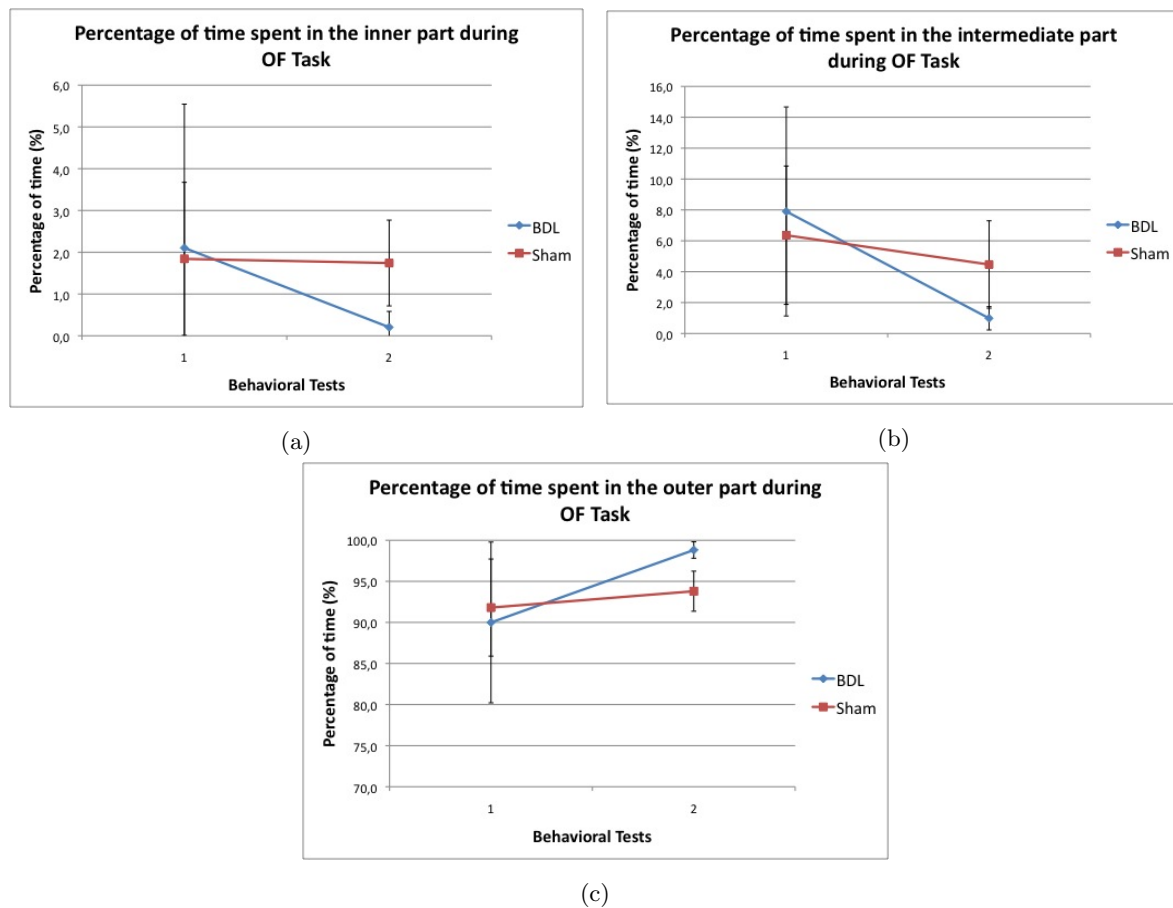

(a)   (b)
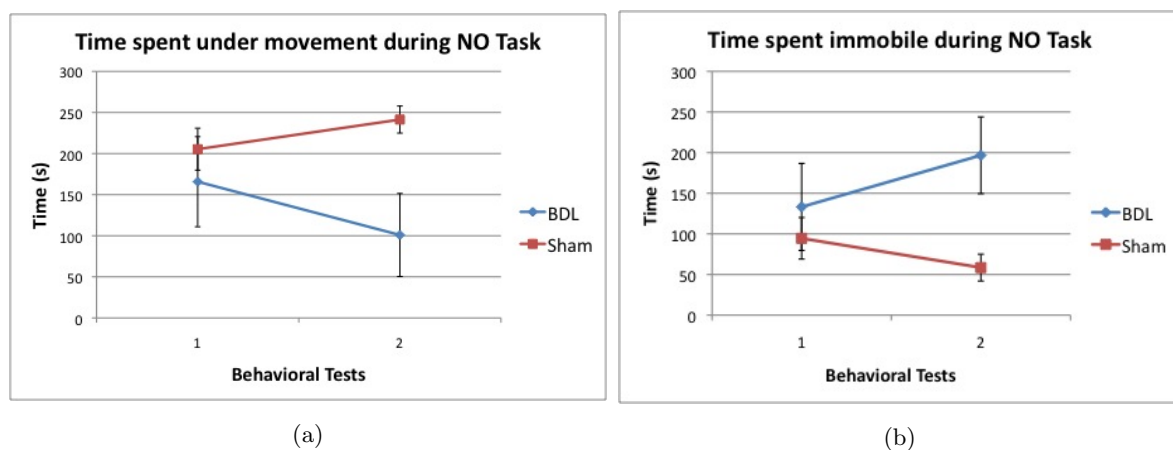
Figure 4.8: Time spent under movement (a) and immobile (b) during the novel object task at two different time points. At the first time point, the BDL group (n=10) was compared with the sham-operated group (n=6). At the second time point, the BDL group (n=5) was compared with the sham-operated group (n=4). The differences were statistically significant at the second time point (p¡0.002).

(a)

(b)

(c)

Figure 4.9: Percentage of time spent in the (a) inner, (b) intermediate and (c) outer parts of the arena during the novel object task at two different time points. At the first time point, the BDL group (n=10) was compared with the sham-operated group (n=6). At the second time point, the BDL group (n=5) was compared with the sham-operated group (n=4). The differences were not statistically significant.
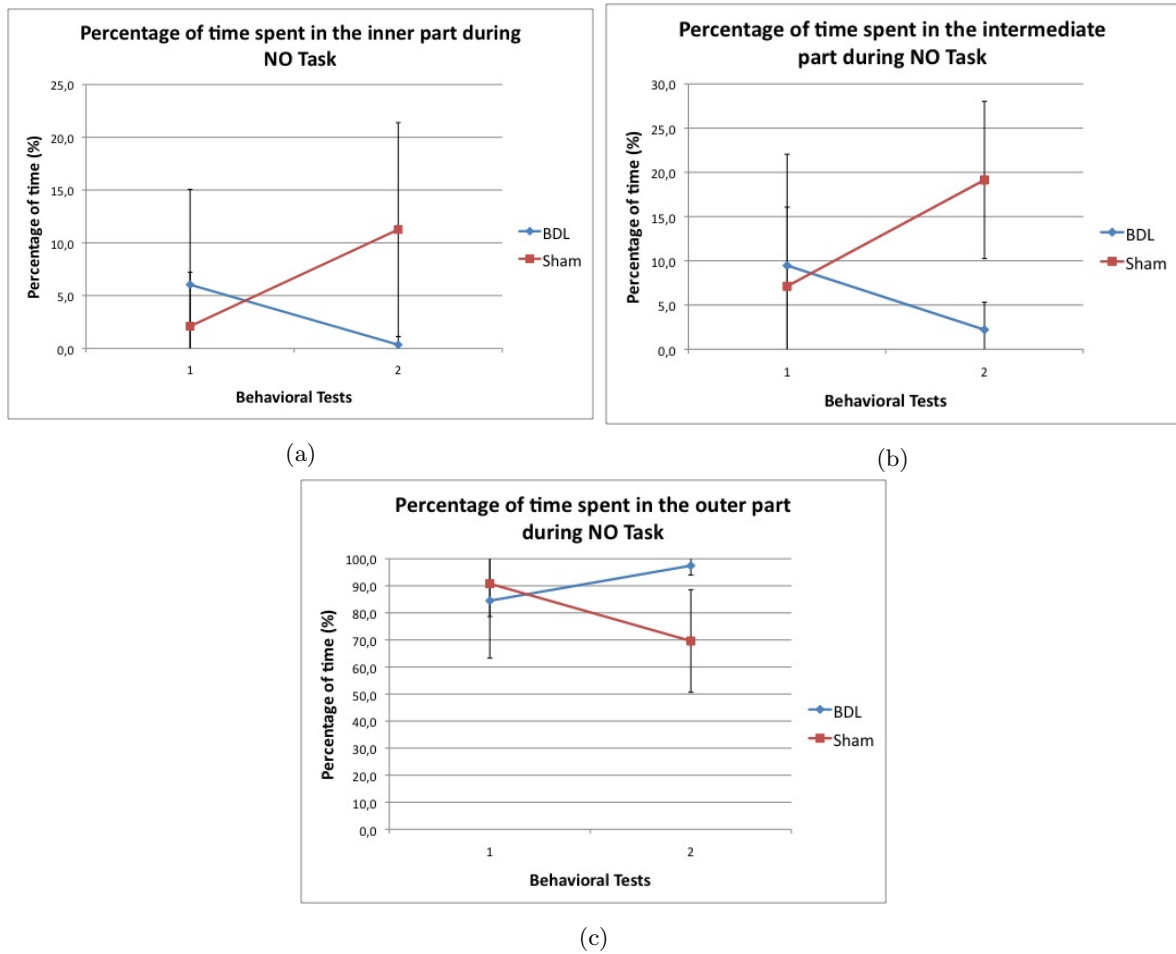
Chapter 5

Discussion and Conclusions

As far as our existing knowledge goes, this is among the first longitudinal ^{31}P MRS studies on brain energy metabolism carried out on a rat model of chronic hepatic encephalopathy. This rather new approach gets together ^{1}H MRS and ^{31}P MRS studies tracking metabolite concentration at several stages of disease and giving insight on cerebral developments over progression of chronic HE. Therefore, it is important to thoroughly understand the processes involved in this study. Some previous *in vivo* MRS studies focused mostly a smaller time frame only with stages after 4 weeks and shorter than 8 weeks (Chavarria et al., 2013). Similarly to the present study, they were done at lower magnetic fields (7T) but just focusing on a small number of metabolites (Gln, Glu, Cr, Cho, Lac, NAA, Ins). The present study was performed ar 9.4T with the detection and tracking changes on 21 metabolites.

5.1 Osmoregulation

Regarding brain osmolyte concentration measured in the present study, an increase in Gln was detected being statistically significant as well as a decrease in tCho and Ins and trends of decreasing concentration levels in Tau and Cr.

Taken together the major increase in Gln and the fact that the total osmolyte concentration (Gln, Ins, Tau, Cr, tCho) was found to remain constant over the time frame of the experiment, suggest an osmoregulatory response equivalent to the Gln increase. As previously mentioned (Heins and Zwingmann, 2010, Cudalbu, 2012), this is a reaction expected in order to compensate the osmotic imbalance induced by Gln accumulation in the astrocytes, as a result of ammonia detoxification in those cells. Additionally and in accordance with previous studies (Laubenberger et al., Cudalbu, 2012), Ins appears as the osmolyte with the most important decrease as a compensatory response to the Gln increase.

5.2   Neurotransmission

A sharp reduction in Asp statistically significant was observed as well as a trend of decrease for Glu. According to the already mentioned studies in Chapter 1, neurotransmission is affected by hyperammonemia. The supply of the neurotransmitter Glu is regulated in the CNS by the Glu - Gln cycle, in which the Gln is synthesized in astrocytes and released to be captured by the transporter SNAT in the brain extracellular space and then captured by neurons to produce Glu. Glu is then released by neurons and taken by astrocytes via the glutamate transporter (GLT-1), therefore completing the cycle. Accordingly, this reduce in Glu may be an evidence of alterations in the outflow of Gln from astrocytes, through a suppression of SNAT as shown in acute HE studies (Kanamori and Ross, 2005). Additionally, the GLT-1 in astrocytes is inactivated when hyperammonemia is present thereby causing increasing extracellular Glu (Albrecht and Jones). Taken together, the above mentioned considerations may nterfere with Glu synthesis.

5.3   Antioxidant Metabolism

A significant decrease was detected in Asc (Vitamin C) and a trend of decrease was observed in GSH. A reduction in antioxidants may indicate the presence of oxidative stress related to ammonia exposure (Bosoi et al., 2012, Braissant, 2010).

5.4   Energy Metabolism

A small trend of decrease observed in γ-ATP is a sign of low potential energy disturbance at week 8. These assumptions are in accordance with previous ^{13}C MRS studies (Lanz et al.), where an increase of pyruvate carboxylase activity was detected with no significant effect on oxidative metabolism or neurotransmission. Therefore, there was no signs of strong effect on energy metabolism. Furthermore, a trend of decrease in Ala was detected as well as a trend of increase in Lac using ^{1}H MRS. An *ex vivo* study showed in 6 weeks BDL rats that a 1.7 fold rise in Lac and not Gln is the main player in the pathogenesis of brain edema in CLD (Bosoi et al., 2014). Our *in vivo* longitudinal results are in contrast with these findings since no significant elevation of Lac in rats 8 weeks following BDL was observed, confirming the findings of others in the same animal model and similar brain region (Chavarria et al., 2013).

5.5   Behavioral Tests

The BDL group of animals presented a lower distance moved statistically significant in both open field and novel object tasks when compared with sham-operated animals. Additionally, the group spent less time under movement and therefore more time immobile, statistically significant. Taken together, the results obtained indicate a lower locomotor activity in the BDL group.

The BDL group presented a tendency not statistically significant for a lower percentage of time spent in the inner part of the arena in comparison with shams. A higher percentage of time

statistically significant spent in the outer part by the BDL group was observed. Therefore, the results indicate a higher anxiety status of BDL group in comparison with sham-operated animals.

5.6   Conclusions

Overall, the present study reinforces that the increase of glutamine responsible for causing the osmotic imbalance, may be in some measure compensated by a coincident decrease of other osmolytes which causes minimal brain oedema. Due to the small alterations in energy metabolites it is not credible that this brain oedema is caused by energy disturbances. Therefore, the most likely cause of minimal brain oedema are the significantly high levels of the osmotically active glutamine concentrations. This supports the *Glutamine Hypothesis* recognized in CLD. One possibility to improve the ^{31}P MRS data is to increase the number of animals in order to have more solid and consistent results that can support this analysis.

Bibliography

Adriany, G. and Gruetter, R. (1997). A Half-Volume Coil for Efficient Proton Decoupling in Humans at 4 Tesla. Journal of Magnetic Resonance, 125(1):178 – 184.

Albrecht, J. and Jones, E. A. Hepatic encephalopathy: molecular mechanisms underlying the clinical syndrome. Journal of the Neurological Sciences, 170(2):138–146.

Albrecht, J. and Norenberg, M. D. (2006). Glutamine: a Trojan horse in ammonia neurotoxicity. Hepatology (Baltimore, Md.), 44(4):788–94.

B. Cady, E. (2012). In Vivo Cerebral 31P Magnetic Resonance Spectroscopy. In Choi, I.-Y. and Gruetter, R., editors, Neural Metabolism In Vivo, chapter 6, pages 149–79. Springer.

Bachmann, C., Braissant, O., Villard, A.-M., Boulat, O., and Henry, H. (2004). Ammonia toxicity to the brain and creatine. Molecular genetics and metabolism, 81 Suppl 1:S52–7.

Bai, G., Rama Rao, K. V., Murthy, C. R., Panickar, K. S., Jayakumar, a. R., and Norenberg, M. D. (2001). Ammonia induces the mitochondrial permeability transition in primary cultures of rat astrocytes. Journal of neuroscience research, 66(5):981–91.

Bak, L. K., Schousboe, A., and Waagepetersen, H. S. (2012). Brain Energy and Ammonia Metabolism, pages 129–144. Bentham Books.

Balcombe, J. P. (2006). Laboratory environments and rodents' behavioural needs: a review. Lab Anim, 40(3):217–235.

Bernstein, M. A., King, K. F., and Zhou, X. J. (2004a). Chapter 14 - Basic Pulse Sequences. In Bernstein, M. A., King, K. F., and Zhou, X. J., editors, Handbook of MRI Pulse Sequences, pages 579 – 647. Academic Press, Burlington.

Bernstein, M. A., King, K. F., and Zhou, X. J. (2004b). Chapter 16 - Echo Train Pulse Sequences. In Bernstein, M. A., King, K. F., and Zhou, X. J., editors, Handbook of MRI Pulse Sequences, pages 702 – 801. Academic Press, Burlington.

Bernstein, M. A., King, K. F., and Zhou, X. J. (2004c). Chapter 2 - Radiofrequency Pulse Shapes. In Bernstein, M. A., King, K. F., and Zhou, X. J., editors, Handbook of MRI Pulse Sequences, pages 35 – 66. Academic Press, Burlington.

Bloch, F. (1946). Nuclear induction. Phys. Rev., 70:460–474.

Bosoi, C. R. and Rose, C. F. (2013a). Brain edema in acute liver failure and chronic liver disease: similarities and differences. Neurochemistry international, 62(4):446–57.

Bosoi, C. R. and Rose, C. F. (2013b). Oxidative stress: a systemic factor implicated in the pathogenesis of hepatic encephalopathy. Metabolic brain disease, 28(2):175–8.

Bosoi, C. R., Yang, X., Huynh, J., Parent-Robitaille, C., Jiang, W., Tremblay, M., and Rose, C. F. (2012). Systemic oxidative stress is implicated in the pathogenesis of brain edema in rats with chronic liver failure. Free radical biology & medicine, 52(7):1228–35.

Bosoi, C. R., Zwingmann, C., Marin, H., Parent-Robitaille, C., Huynh, J., Tremblay, M., and Rose, C. F. (2014). Increased brain lactate is central to the development of brain edema in rats with chronic liver disease. Journal of hepatology, 60(3):554–60.

Braissant, O. (2010). Current concepts in the pathogenesis of urea cycle disorders. Molecular genetics and metabolism, 100 Suppl:S3–S12.

Braissant, O., McLin, V. a., and Cudalbu, C. (2012). Ammonia toxicity to the brain. Journal of Inherited Metabolic Diseases, 36(4):595–612.

Brusilow, S. W., Koehler, R. C., Traystman, R. J., and Cooper, A. J. L. (2010). Astrocyte glutamine synthetase: importance in hyperammonemic syndromes and potential target for therapy. Neurotherapeutics : the journal of the American Society for Experimental NeuroTherapeutics, 7(4):452–70.

Butterworth, R. F. (2003). Pathogenesis of hepatic encephalopathy: new insights from neuroimaging and molecular studies. Journal of Hepatology, 39(2):278–285.

Butterworth, R. F., Norenberg, M. D., Felipo, V., Ferenci, P., Albrecht, J., Blei, A. T., and of the ISHEN Commission on Experimental Models of HE], M. (2009). Experimental models of hepatic encephalopathy: Ishen guidelines. Liver International, 29(6):783–788.

Cagnon, L. and Braissant, O. (2007). Hyperammonemia-induced toxicity for the developing central nervous system. Brain research reviews, 56(1):183–97.

Chan, P. and Fishman, R. (1985). Brain edema. In Lajtha, A., editor, Pathological Neurochemistry, pages 153–174. Springer US.

Chavarria, L., Oria, M., Romero-Giménez, J., Alonso, J., Lope-Piedrafita, S., and Cordoba, J. (2013). Brain magnetic resonance in experimental acute-on-chronic liver failure. Liver international : official journal of the International Association for the Study of the Liver, 33(2):294–300.

Chen, C.-N., Hoult, D., and Sank, V. (1983). Quadrature detection coils - a further $\sqrt{2}$ improvement in sensitivity. Journal of Magnetic Resonance (1969), 54(2):324 – 327.

Cudalbu, C. (2012). In vivo studies of brain metabolism in animal models of hepatic encephalopathy using 1h magnetic resonance spectroscopy. Metabolic brain disease, 28(2):167–74.

Dalrymple-Alford, J. C. and Benton, D. (1984). Behavioural inhibition and the age at social isolation in rats. The Quarterly Journal of Experimental Psychology Section B, 36(1):27–38.

Desjardins, P., Du, T., Jiang, W., Peng, L., and Butterworth, R. F. (2012). Pathogenesis of hepatic encephalopathy and brain edema in acute liver failure: role of glutamine redefined. Neurochemistry international, 60(7):690–6.

Felipo, V. (2013). Hepatic encephalopathy: effects of liver failure on brain function. Nature reviews. Neuroscience, 14(12):851–8.

Ferenci, P., Lockwood, A., Mullen, K., Tarter, R., Weissenborn, K., and Blei, A. T. (2002). Hepatic encephalopathy–definition, nomenclature, diagnosis, and quantification: final report of the working party at the 11th World Congresses of Gastroenterology, Vienna, 1998. Hepatology (Baltimore, Md.), 35(3):716–21.

Gallagher, T. A., Nemeth, A. J., and Hacein-Bey, L. (2008). An introduction to the fourier transform: Relationship to mri. American Journal of Roentgenology, 190(5):1396–1405.

gon Lee, H., Casadesus, G., Perry, G., Bryan, K., and Smith, M. (2008). Transgenic Mouse Models of Alzheimer's Disease, pages 1–18. Frontiers in neuroscience. CRC Press, 2nd ed. edition.

Govindaraju, V., Young, K., and Maudsley, A. A. (2000). Proton NMR chemical shifts and coupling constants for brain metabolites. NMR in Biomedicine, 13(3):129–153.

Graaf, R. A. D. (2007). In Vivo NMR Spectroscopy. Wiley, 2nd edition.

Gruetter, R. (1993). Automatic, localized in vivo adjustment of all first and second order shim coils. Magnetic Resonance in Medicine, 29:804–811.

Gruetter, R. and Tkac, I. (2000). Field mapping without reference scan using asymmetric echo-planar techniques. Magnetic Resonance in Medicine, 43(2):319–323.

Gutierrez, J., Ballinger, S. W., Darley-Usmar, V. M., and Landar, A. (2006). Free radicals, mitochondria, and oxidized lipids: the emerging role in signal transduction in vascular cells. Circulation research, 99(9):924–32.

Haghighat, N. and McCandless, D. W. (1997). Effect of ammonium chloride on energy metabolism of astrocytes and C6-glioma cells in vitro. Metabolic brain disease, 12(4):287–98.

Haghighat, N., McCandless, D. W., and Geraminegad, P. (2000). The effect of ammonium chloride on metabolism of primary neurons and neuroblastoma cells in vitro. Metabolic brain disease, 15(2):151–62.

Heales, S. J., Bolaños, J. P., Stewart, V. C., Brookes, P. S., Land, J. M., and Clark, J. B. (1999). Nitric oxide, mitochondria and neurological disease. Biochimica et biophysica acta, 1410(2):215–28.

Heins, J. and Zwingmann, C. (2010). Organic osmolytes in hyponatremia and ammonia toxicity. Metabolic Brain Disease, 25(1):81–89.

Hennig, J., Nauerth, A., and Friedburg, H. (1986). RARE imaging: A fast imaging method for clinical MR. Magnetic Resonance in Medicine, 3(6):823–833.

Hindfelt, B., Plum, F., and Duffy, T. (1977). Effect of acute ammonia intoxication on cerebral metabolism in rats with portacaval shunts. Journal of Clinical Investigation, 59(September 1976):386–396.

Jover, R., Rodrigo, R., Felipo, V., Insausti, R., Sáez-Valero, J., García-Ayllón, M. S., Suárez, I., Candela, A., Compañ, A., Esteban, A., Cauli, O., Ausó, E., Rodríguez, E., Gutiérrez, A., Girona, E., Erceg, S., Berbel, P., and Pérez-Mateo, M. (2006). Brain edema and inflammatory activation in bile duct ligated rats with diet-induced hyperammonemia: A model of hepatic encephalopathy in cirrhosis. Hepatology (Baltimore, Md.), 43(6):1257–66.

Kala, G. and Hertz, L. (2005). Ammonia effects on pyruvate/lactate production in astrocytes–interaction with glutamate. Neurochemistry international, 47(1-2):4–12.

Kale, R. a., Gupta, R. K., Saraswat, V. a., Hasan, K. M., Trivedi, R., Mishra, A. M., Ranjan, P., Pandey, C. M., and Narayana, P. a. (2006). Demonstration of interstitial cerebral edema with diffusion tensor MR imaging in type C hepatic encephalopathy. Hepatology (Baltimore, Md.), 43(4):698–706.

Kanamori, K. and Ross, B. D. (2005). Suppression of glial glutamine release to the extracellular fluid studied in vivo by nmr and microdialysis in hyperammonemic rat brain. Journal of Neurochemistry, 94(1):74–85.

Karim, A. and Arslan, M. I. (2000). Isolation modifies the behavioural response in rats. Bangladesh Med Res Counc Bull, 26(1):27–32.

Keiding, S. and Pavese, N. (2013). Brain metabolism in patients with hepatic encephalopathy studied by PET and MR. Archives of biochemistry and biophysics, 536(2):131–42.

Kristal, B. S. and Dubinsky, J. M. (1997). Mitochondrial permeability transition in the central nervous system: induction by calcium cycling-dependent and -independent pathways. Journal of neurochemistry, 69(2):524–38.

Kunz, N. (2010). Biophysical Basis of the Diffusion-Weighted Magnetic Resonance Signal in the Rat Brain. (March).

Lai, J. and Cooper, A. (1991). Neurotoxicity of ammonia and fatty acids: Differential inhibition of mitochondrial dehydrogenases by ammonia and fatty acyl coenzyme a derivatives. Neurochemical Research, 16(7):795–803.

Lanz, B. (2012). Mathematical Modeling of Brain Energy Metabolism, Measured with PET and MRS in Rodents. PhD thesis.

Lanz, B., Cudalbu, C., McLin, V., Lepore, M., Braissant, O., and Gruetter, R. In vivo ^{13}C MRS investigation of alterations in cerebral oxidative metabolism in a chronic liver disease rat model. In Conference proceedings, CIBM/LIFMET, Salt Lake City, USA, 2013.

Laubenberger, J., Haussinger, D., Bayer, S., Gufler, H., Hennig, J., and Langer, M. Proton magnetic resonance spectroscopy of the brain in symptomatic and asymptomatic patients with liver cirrhosis. Gastroenterology, 112(5):1610–1616.

Leke, R., Bak, L. K., Anker, M., Melø, T. M., Sø rensen, M., Keiding, S., Vilstrup, H., Ott, P., Portela, L. V., Sonnewald, U., Schousboe, A., and Waagepetersen, H. S. (2011). Detoxification of ammonia in mouse cortical GABAergic cell cultures increases neuronal oxidative metabolism and reveals an emerging role for release of glucose-derived alanine. Neurotoxicity research, 19(3):496–510.

Mardini, H., Smith, F. E., Record, C. O., and Blamire, A. M. (2011). Magnetic resonance quantification of water and metabolites in the brain of cirrhotics following induced hyperammonaemia. Journal of hepatology, 54(6):1154–60.

Mckenna, M. C., Dienel, G. A., Sonnewald, U., Waagepetersen, H. S., and Schousboe, A. (2012). Energy Metabolism of the Brain. pages 200–231.

McKhann, G. and Tower, D. (1961). Ammonia toxicity and cerebral oxidative metabolism. Am. J. Physiol.

Mcphail, M. J. W., Thomas, H. C., and Taylor-robinson, S. D. (2012). Magnetic Resonance Studies of the Brain in Liver Disease. In Keiding, S. and Sorensen, M., editors, Functional Molecular Imaging in Hepatology, chapter 15, pages 160–182. Bentham Science Publishers.

Mlynarik, V. (2016). Introduction to nuclear magnetic resonance. Analytical Biochemistry.

Mlynarik, V., Cacquevel, M., Sun-Reimer, L., Janssens, S., Cudalbu, C., Lei, H., Schneider, B. L., Aebischer, P., and Gruetter, R. (2012). Proton and phosphorus magnetic resonance spectroscopy of a mouse model of alzheimer's disease. Journal of Alzheimer's Disease, 31 Suppl 3:S87–99. ID: unige:33000.

Mlynárik, V., Gambarota, G., Frenkel, H., and Gruetter, R. (2006). Localized short-echo-time proton MR spectroscopy with full signal-intensity acquisition. Magnetic Resonance in Medicine, 56(5):965–70.

Moratal, D., Vallés-Luch, A., Martí-Bonmatí, L., and Brummer, M. (2008). k-space tutorial: an mri educational tool for a better understanding of k-space. Biomedical Imaging and Intervention Journal, 4(1):e15.

Munoz, S. J. (2008). Hepatic encephalopathy. The Medical clinics of North America, 92(4):795–812, viii.

Murthy, C. and Rao, K. R. (2001). Ammonia induced production of free radicals in primary cultures of rat astrocytes. Journal of neuroscience research, 66:282–288.

Ordidge, R., Connelly, A., and Lohman, J. (1986). Image-selected in Vivo spectroscopy (ISIS). A new technique for spatially selective NMR spectroscopy. Journal of Magnetic Resonance (1969), 66(2):283 – 294.

Oria, M. and Jalan, R. (2014). Brain lactate in hepatic encephalopathy: friend or foe? Journal of hepatology, 60(3):476–7.

Provencher, S. W. (2001). Automatic quantitation of localized in vivo ^{1}H spectra with LCModel. NMR in Biomedicine, 14(4):260–264.

Qureshi, K., Rao, K. V., and Qureshi, I. a. (1998). Differential inhibition by hyperammonemia of the electron transport chain enzymes in synaptosomes and non-synaptic mitochondria in ornithine transcarbamylase-deficient spf-mice: restoration by acetyl-L-carnitine. Neurochemical research, 23(6):855–61.

Rama Rao, K. V., Jayakumar, a. R., and Norenberg, M. D. (2005). Differential response of glutamine in cultured neurons and astrocytes. Journal of neuroscience research, 79(1-2):193–9.

Rama Rao, K. V. and Norenberg, M. D. (2012). Brain energy metabolism and mitochondrial dysfunction in acute and chronic hepatic encephalopathy. Neurochemistry international, 60(7):697–706.

Rama Rao, K. V. and Norenberg, M. D. (2014). Glutamine in the pathogenesis of hepatic encephalopathy: the trojan horse hypothesis revisited. Neurochemical research, 39(3):593–8.

Rao, K. and Norenberg, M. (2001). Cerebral energy metabolism in hepatic encephalopathy and hyperammonemia. Metabolic Brain Disease, 16(June):67–78.

Rao, K. V., Mawal, Y. R., and Qureshi, I. a. (1997). Progressive decrease of cerebral cytochrome C oxidase activity in sparse-fur mice: role of acetyl-L-carnitine in restoring the ammonia-induced cerebral energy depletion. Neuroscience letters, 224(2):83–6.

Ringel, F., Baethmann, A., and Plesnila, N. (2006). Lactacidosis-induced glial cell swelling depends on extracellular Ca^{2+}. Neuroscience letters, 398(3):306–9.

Rose, C. F. (2010). Increase brain lactate in hepatic encephalopathy: cause or consequence? Neurochemistry international, 57(4):389–94.

Rovira, a., Alonso, J., and Córdoba, J. (2008). MR imaging findings in hepatic encephalopathy. American journal of neuroradiology, 29(9):1612–21.

Singh, S., Mondal, P., and Trigun, S. K. (2014). Acute liver failure in rats activates glutamine-glutamate cycle but declines antioxidant enzymes to induce oxidative stress in cerebral cortex and cerebellum. PloS one, 9(4).

Stewart, V. C., Sharpe, M. a., Clark, J. B., and Heales, S. J. (2000). Astrocyte-derived nitric oxide causes both reversible and irreversible damage to the neuronal mitochondrial respiratory chain. Journal of neurochemistry, 75(2):694–700.

Tannús, a. and Garwood, M. (1997). Adiabatic pulses. NMR in biomedicine, 10(8):423–34.

Vanhamme, L., Sundin, T., Hecke, P. V., and Huffel, S. V. (2001). MR spectroscopy quantitation: a review of time-domain methods. NMR in Biomedicine, 14(4):233–246.

Weissenborn, K. and Lockwood, A. H. (2012). Cerebral Glucose Metabolism in Patients with Liver Cirrhosis and Hepatic Encephalopathy, pages 145–152. Bentham Books.

Xue, Z., Li, B., Gu, L., Hu, X., Li, M., Butterworth, R. F., and Peng, L. (2010). Increased Na, K-ATPase alpha2 isoform gene expression by ammonia in astrocytes and in brain in vivo. Neurochemistry international, 57(4):395–403.

Zorov, D. B., Juhaszova, M., and Sollott, S. J. (2006). Mitochondrial ROS-induced ROS release: an update and review. Biochimica et biophysica acta, 1757(5-6):509–17.

Zwingmann, C. (2007). Nuclear magnetic resonance studies of energy metabolism and glutamine shunt in hepatic encephalopathy and hyperammonemia. Journal of neuroscience research, 3442(August):3429–3442.

Zwingmann, C. and Leibfritz, D. (2005). Ammonia toxicity under hyponatremic conditions in astrocytes: de novo synthesis of amino acids for the osmoregulatory response. Neurochemistry international, 47(1-2):39–50.